WAVELENGTH MODULATION SPECTROSCOPY OF SEMICONDUCTORS

Stanley Erwin Kohn

ABSTRACT

The use of modulation spectroscopy to study the electronic properties of solids has been very productive. The construction of a wide range Wavelength Modulation Spectrometer to study the optical properties of solids is described in detail. Extensions of the working range of the spectrometer into the vacuum ultraviolet are discussed. Measurements of the reflectivity and derivative reflectivity spectra of the lead chalcogenides, the chalcopyrite $ZnGeP_2$, the layer compounds GaSe and GaS and their alloys, the ferroelectric SbSI, layer compounds SnS_2 and $SnSe_2$, and HfS_2 were made. The results of these measurements are presented along with their interpretation in terms of band structure calculations.

ACKNOWLEDGEMENTS

There are numerous people whose kindness and assistance were very helpful to me in my research. Foremost among them is my thesis adviser, Professor Y. R. Shen, to whom I am deeply indebted.

WAVELENGTH MODULATION SPECTROSCOPY OF SEMICONDUCTORS

TABLE OF CONTENTS

I. INTRODUCTION

Ever since the beginnings of the quantum theory of solids in the 1930's, one of the goals of solid state physics has been to determine the quantum states of solids both experimentally and theoretically. Very early, theorists learned to separate the eigenstates of crystalline materials into separate systems of electronic and phonon states by the Born-Oppenheimer approximation. By using Hartree and Hartree-Foch approaches to the many-body electronic problem, theorists were able to write an approximate one-electron Hamiltonian equation with an effective potential that includes electromagnetic interactions, exchange interactions and correlation interactions. By modeling this potential, and by expanding the one-electron eigenfunctions into a set of complete functions, several empirical methods for solving the Hamiltonian equation were developed by Slater,[1] Herring,[2] and Phillips.[3]

However, little experimental information about the electronic states away from the Fermi level was available until the 1960's. Up until that time, many techniques for studying the transport properties of solids had given considerable information about electronic states near the Fermi level.

Two major advances changed that. First in 1959, Philipp and Taft[4] performed the first accurate measurements of the normal-incidence reflectivity of semiconductors. By doing a Kramers-Kronig analysis of their data, they learned about the energy and symmetry of many interband transitions of their samples. This was the first example where the relectivity was used to give reliable information about electronic states of solids.

The problem with reflectivity measurements is that the observed struc-

tures are usually very broad and are on top of a large background. The second major advance was the development of the technique of modulation spectroscopy by Seraphin.[5] By modulating a parameter of the system, a derivative spectrum is measured and the critical points in the optical properties of the sample can be more readily identified and studied. Seraphin pioneered the technique of electric field modulation. Since then, others have developed methods of pressure[6] and temperature[7] modulation. At Berkeley, Zucca and Shen[8] developed the technique of wavelength modulation spectroscopy (WMS).

With these different techniques of modulation spectroscopy, numerous workers have examined the optical properties of many materials.[9] The earliest work was done on the group IV elements Si and Ge and the groups III-V semiconductors. The work reported here is an expansion of the technique of wavelength modulation spectroscopy to many other materials — layer compounds, lead chalcogenides, chalcopysites, and ferroelectrics.

For a number of experimental reasons, most of the previously reported modulation spectroscopy has been limited to the spectral range from the near ultraviolet to the near infrared (approximately 0.2 μm to 5 μm). For most of the group IV and the III-V semiconductors, many of the major features of the optical spectrum are in this region. However, as one progresses to the II-VI and I-VII compounds, the energy gaps get much larger and more of the interesting features of the optical spectrum are in the vacuum ultraviolet. For this reason, part of the original motivation for this research was to extend the accessible experimental region farther into the ultraviolet. Alas, the results of that part of this work were not very successful.

Nevertheless, considerable information about the electronic proper-

ties of several different compounds was obtained. Much of this work was done in association with the theoretical solid state physicists at Berkeley led by M. L. Cohen. They performed empirical pseudopotential band structure calculations on the same compounds. Usually, the reflectivity and derivative reflectivity spectra were not used for the empirical fitting procedure, but for comparison to decide the accuracy of the theoretical calculations.

II. EXPERIMENTAL DESCRIPTION

Wavelength modulation spectroscopy, like any other modulation technique, involves modulating a physical parameter of the system, x, at a frequency ω. If the modulation amplitude is small and if the modulation is sinusoidal, then the signal, S(x), can be expanded in a Taylor series of the modulated parameter

$$S(x) = S(x_0) + A \frac{dS}{dx}(x_0)\cos \omega t + \ldots \quad (1)$$

where A is the modulation amplitude. For wavelength modulation spectroscopy, x is the wavelength of the light passing through the monochrometer. A detailed derivation of the wavelength modulation signal, including the effects of monochrometer resolution, has been done by Zucca.[8] The simple form of Eq. (1) is valid as long as

$$A^2 \ll \Delta^2 \text{ and } W^2 \ll \Delta^2 \quad (2)$$

where Δ is the width of the narrowest spectral feature and W is the slit width of the monochrometer.

The main difficulty in doing WMS is that the signal measured is the derivative of the entire optical system and not just the derivative of the sample reflectivity (or transmission). Thus, it is necessary for us to employ feedback servo loops to cancel the background signal due to the optical response of the rest of the system. It is also very important to avoid sharp spectral structures, such as atomic-like emission lines in the light source. Such sharp structures can have such an enor-

mous derivative signal that the feedback servo systems are overloaded.

A. Wavelength Modulation

The optical system for the entrance to the monochrometer is shown in Fig. 1. Light from lamp L is focused by mirror M1 onto slit S1. Slit S1 is external to the monochrometer but acts as effective entrance slit for the monochrometer. Light from slit S1 is reflected by mirror M2 and focused by mirror M3 onto the normal slit of the monochrometer, S2. The effective slit, S1, was usually opened to approximately ½ mm. The normal monochrometer entrance slit, S2, was open as wide as possible (about 4 mm). The monochrometer is a standard ½ meter Ebert optical mount. Mirror M2 is a commercial torsion-bar vibrating mirror[10] operating at a frequency of 6 KHz. The mirror vibrates as shown in Fig. 1 by the small arrow. Because of this vibration, the image of slit S1 vibrates across the wide open slit S2. The effect is to move the source spot for the diffraction grating optics. Therefore, the "rainbow" produced by the diffraction grating across the monochrometer exit slit, S3, oscillates in space at the modulation frequency. Thus the wavelength of light coming out of the monochrometer will have a central wavelength modulated at 6 KHz. If the monochrometer optics are properly focused, the exit beam will not oscillste in space. If A is the amplitude of the motion of the image at slit S2, then exit central wavelength will be

$$\lambda = \lambda_0 + A \frac{d\lambda}{dx} \cos \omega t \qquad (3)$$

where $\frac{d\lambda}{dx}$ is the dispersion of the monochrometer. After the wavelength modulated data is recorded, a small correction is made to the signal

amplitude to correct for the variation of the monochrometer dispersion with wavelength.

B. Optical System

The optical system for the sample and detector are shown in Fig. 2. This is an accurate double beam system with separate sample and reference beams. The light emerging from the monochrometer is focused by mirrors M4 and M5 onto chopper mirror M6. The chopper mirror is a circular mirror with two opposite quadrants cut away and rotated by a 5 Hz motor. When the beam passes through the chopper mirror, it is focused onto the sample by elliptical mirror M7. The sample sits in a helium cryrostat that is not shown in the figure. The light reflected from the sample is collected by mirror M8 and focused onto the photomultiplier detector (EMI 9558). When the chopper mirror reflects the light from mirror M4, it is focused by mirror M9 onto the same photomultiplier. This beam, the reference beam, passes through four windows to compensate for the windows on the helium cryrostat. Thus, the photomultiplier alternately detects the sample beam and then from the reference beam. For work in the vacuum ultraviolet region of the spectrum, a microscope slide coated with sodium salicylate is placed in front of the photomultiplier. Sodium salicylate is a very efficient fluorescent material.[11] It is sensitive to radiation from approximately 275 Å to 4000 Å. The fluorescent emission is in a band about 1000 Å wide centered around 4200 Å. The quantum efficiency is believed to be near 60%.

With the exception of the lamp and cryrostat windows, all of the optical elements of the system are mirrors coated with aluminum and overcoated with magnesium flouride. Therefore, there are no chromatic abera-

tion effects. Aluminum mirrors overcoated with magnesium flouride are known to have high reflectivity from about 1200 Å to the infrared.[12]

C. Electronic Instrumentation

A block diagram of the electronics is given in Fig. 3. After the pre-amplifier, the sample and reference signals are separated by a pair of mercury relays operated synchronously with the chopper mirror. The first relay provides a small dead time to eliminate spikes in the signal caused by the edges of the chopper mirror. The other relay switches the signal to the appropriate processing electronics. Each signal channel has a "DC" amplifier and a lock-in amplifier (Princeton Applied Research, Inc., models HR-8 and 124). The "DC" amplifiers detect the 10 Hz signals proportional to the average value of the optical signals, while the lock-in amplifiers detect the signals at the 6 KHz modulation frequency. If we denote by I the reference signals and by R the reflectivity (or transmission) of the sample, then the four measured signals are proportional to

	"DC"	6 KHz "AC"	
Reference	I	$\frac{dI}{d\lambda}\,\Delta\lambda$	(4)
Sample	IR	$\frac{d}{d\lambda}\,(IR)\,\Delta\lambda$	

where $\Delta\lambda$ is the modulation amplitude.

Two feedback loops, described below, are used to normalize the signals. One feedback loop is used to keep the reference DC signal equal

to a constant, c. If the other feedback loop is used to set the reference 6 KHz signal to zero, then the sample 6 KHz signal will be proportional to $c \frac{dR}{d\lambda} \Delta\lambda$. However, the usual arrangement was to use the second feedback loop to set the sample 6 KHz signal to zero. In that case, the reference 6 KHz signal is proportional to $-\frac{1}{c} \frac{dR}{Rd\lambda}$.

D. Feedback Loops

A schematic of the pre-amplifier and part of the 6 KHz feeback loop is shown in Fig. 4. A constant bias voltage, c, is subtracted from the signal by the second amplifier. This bias voltage is provided by a mercury battery. The output from the reference DC amplifier is then applied to an integrator. The output of the integrator varies the high voltage bias supply for the photomultiplier. The steady state condition is reached when the input to the integrator is zero, i.e. when I equals c. This is the first feedback servo loop.

The output from the sample lock-in amplifier, which is the signal to be nulled for the second feedback loop, is applied to another integrator. The output of the integrator amplitude modulates a 6 KHz carrier wave. This carrier wave is used to control the gain of the first stage of the preamplifier. The gain of the first stage amplifier of the preamplifier is

$$G = \frac{1}{R_1} \left(R_2 + R_3 + \frac{R_3 R_2}{R_{FET}} \right) \qquad (5)$$

Where R_{FET} is the channel resistance of the FET transistor. It is empirically known that the channel resistance of a FET is approximately

$$R_{FET} \approx \frac{R_0}{1 - KV_{GATE}} . \tag{6}$$

If a voltage at frequency ω is applied to the gate of the FET, then, we can write the gain of this amplifier as

$$G = G_0(1 + A \cos \omega t) \tag{7}$$

where G_0 is a fixed constant and A is proportional to the magnitude of the gate voltage. Then, to first order in $\cos \omega t$, the four signals emerging from the preamplifier will be proportional to

	DC	6 KHz "AC"
Reference	$I - c$	$\frac{dI}{d\lambda}\Delta\lambda + AI$
Sample	$IR - c$	$\frac{d}{d\lambda}(IR)\Delta\lambda + AIR$.

(8)

If the reference DC signal and the sample 6 KHz signal are set to zero by means of the feedback loops, then the sample DC signal will be proportional to

$$c(R - 1) \tag{9}$$

and the reference 6 KHz signal will be proportional to

$$-\frac{c}{R}\frac{dR}{d\lambda}\Delta\lambda = -c\frac{\Delta R}{R} . \tag{10}$$

These are the signals recorded.

It is important that the phases of both of the lock-in amplifiers and of the 6 KHz feedback be adjusted properly. If θ is the phase of the 6 KHz feedback signal relative to the phase of the reference channel lock-in amplifier, and if ϕ is the relative phase of the sample channel lock-in amplifier, then the recorded signal is

$$- c \frac{R}{R} + A \cos \theta(1 - \sec \phi). \qquad (11)$$

Note, if ϕ equals zero, i.e. if both lock-ins are in phase, then phase of the 6 KHz feedback is not critical.

E. Light Sources

Because both the sample and reference channel signals contain the derivative of the lamp spectrum, it is important that the lamp have a smooth continuum spectrum. For this reason, three different lamps were used in different regions of the optical spectrum. In the visible and near infrared, a quartz enveloped tungsten-halogen lamp is used. The particular lamp used is of the type used for commercial slide projectors (ANSI type FDS). This lamp has a very smooth continuum usable from about 3500 Å to the infrared. In the region from 2000 Å to 4500 Å, a 75 watt high pressure xenon short arc lamp is used (Illumination Industries Inc., model III-76). In this spectral region, the intensity is reasonably smooth, although in some individual lamps trace impurities of mercury can give strong lines. In the visible and infrared regions of the spectrum, a xenon lamp is actually more intense than a tungsten-halogen lamp, however, it has many sharp structures that overload the feedback systems

in WMS.

For use in the vacuum ultraviolet region of the spectrum, I constructed a 200 watt cooled deuterium lamp. Molecular hydrogen and deuterium are known experimentally to have a continuum emission spectrum around 2000 Å. It is believed that this continuum arises from transistion from $^2\Sigma_g^+$ excited bonding state to the $^3\Sigma_u^+$ anti-bonding state.[13] Since the energy of the $^3\Sigma_u^+$ anti-bonding state is a smoothly decreasing function of the inter-nuclear distance, a continuum of final states exists, and hence a continuum emission spectra is possible. At higher energies, the emission spectrum of the lamp is composed of a large number of lines originating from many different electronic transitions of the D_2 molecule and the vibrational sub-bands of the transitions.

A schematic drawing of the deuterium lamp is shown in Fig. 5. The base of the lamp is a stainless steel Conflat vacuum flange. Three electrical feedthroughs are made on this flange by using ceramic to cover end seals. A molybdenum anode is attached to the center feedthrough. The other two feedthroughs are connected to a filament. The filament is a commercial dispenser tungsten filament (Spectra Mat, Inc., model TB-112-8) designed to give a very high electron emission. The electrons excite the D_2 molecules into the $^2\Sigma_g^+$ state. Other filaments were tried. Nickel wire coated with a mixture of $BaCO_3$ and $SrCO_3$ gives a very high electron emission, but a large ion current which strikes the filament can eat through the nickel in a matter of a few minutes. Plain tungsten filaments require a much higher temperature to achieve sufficient electron emission.

In between the anode and the filament there is a molybdenum cylinder with a 1 mm diameter hole in the middle. This cylinder is supported by

ceramic piece so that it is electrically isolated from the anode and the filament. This cylinder serves to confine and to stabilize the plasma discharge between the anode and the filament. The 1 mm hole acts as a small optical light source.

The mating flange to the base has welded onto it a nickel plated stainless steel can. Around this can is a water cooling jacket. A lithium flouride window is epoxied onto the other end of the can. The water jacket serves to cool the window and the gas between the window and the filament. This is necessary to prevent the formation of color centers in the lithium flouride window.

The electrical circuit for the lamp is similar to that for a conventional discharge lamp. A 3500 volt DC power supply provides a bias between the anode and the filament through a variable 500 ohm ballast resistor. A separate power supply is used to heat the filament to approximately 1500° C. After the discharge is initiated with a Tesla coil applied to the anode lead, the voltage directly across the lamp drops to about 110 volts. The ballast resistor is then adjusted so that about 1.5 amps is drawn by the lamp. The gas pressure is adjusted to give maximum light intensity. This occurs at a pressure of about 6 torr. Under these conditions, there is a very strong ion current from the anode to the filament. This ion current is sufficiently powerful to heat the filament to the operating temperature. It is then possible to turn off the filament current after the lamp discharge has started. The ion current slowly destroys the filament. After about 50 hours of operation, I found it necessary to recoat the filament with a mixture of $BaCO_3$ and $SrCO_3$. The recoated filament is then slowly heated in vacuum to reduce the $BaCO_3$ to BaO.

A spectrum of this lamp is shown in Fig. 5. This spectrum has not been corrected for dispersion of the optical response of the rest of the system. The continuum around 2000 Å is adequate for doing wavelength modulation spectroscopy. At shorter wavelengths, around 1500 Å, the multi-line molecular spectra of deuterium is broadened into an apparent continuum. This apparent broadening is due to the lamp pressure (~ 6 mm) and the resolution of the optical system (~ 10 Å).

F. Data Processing

The measured signals, $R(\lambda)$ and $1/R\ dR/d\lambda$, were digitized and recorded on a magnetic tape for later signal processing. The recording system consisted of an anologue switch which alternated between the two data channels, a digital panel meter to digitize the data, an incremental magnetic tape drive to record the data, and a controller. Since the pass wavelength of the monochrometer was scanned at a constant rate, the controller needed only to be primarily a clock to command the system to record data periodically. However, the clock was triggered by the event marker relay of the monochrometer, which gave a pulse every 10 Å. Thus, even if the clock were only accurate and stable to 10%, a wavelength accuracy of 1 Å could be maintained and there would be no cumulative error over a scan of many thousands of Ångstroms.

Once the data has been transferred to a computer, three calculations are done. First, a small correction is made to the signal amplitude to correct for wavelength dependence of the monochrometer dispersion. For an Ebert mounting of focal length f, the inverse linear dispersion is[14]

$$\frac{d\lambda}{dx} = \frac{2d}{f}\left[\left(1 - \left(\frac{\lambda}{2d}\right)^2\right)^{\frac{1}{2}} + \frac{\lambda}{2d}\,\frac{\ell}{2f}\right] \qquad (12)$$

where d is the spacing between grating grooves and ℓ is the distance between the entrance and exit slits. This correction is of the order of 5%.

Secondly, a correction for an apparent zero shift of the derivative data is sometimes necessary. Various non-linearities in the optical system and some differences in the sample and reference beams can add components to the derivative signals. Unfortunately, not all of these effects are understood. These effects include harmonic distortions in the modulation and optical abberations in the monochrometer which modulate different parts of the light beam differently. Proper optical alignment, particularly of the optics on the entrance to the monochrometer, could minimize these effects. To correct for the zero shift, an adjustable straight line was added to the derivative data. The derivative data is then integrated and compared with the measured reflectivity. The straight line is adjusted by a small amount until the integrated derivative data match the measured reflectivity.

The final step in the data processing is to convert the data from wavelength to energy.

G. Kramers Krönig Analysis

When doing theoretical calculations, the most simple and informative optical function that is calculated is ε_2, the imaginary part of the dielectric function. As is well known for interband electronic transitions, ε_2 is approximately

$$\varepsilon_2(\omega) \propto |\langle i|p|f\rangle|^2 D(\omega) \qquad (13)$$

where $\langle i|p|f\rangle$ is the dipole matrix element for this transition and $D(\omega)$ is the joint density of states. Unfortunately, the measured linear optical functions, the reflectivity or the transmission, are not simply related to ϵ_2. In principle, to calculate R or T from theoretical calculations requires knowledge of both the real and imaginary parts of ϵ. Similarly, to calculate ϵ from R or T requires knowledge of both R and T or knowledge of either R and T and the phase of the reflected or transmitted wave relative to the incident wave. Rarely are any of these situations satisfied.

One way around this is to do a Kramers-Krönig analysis of R or T to find the phase difference. If we write the reflectivity as the modules of a complex reflectivity,

$$R = |\rho e^{i\theta}|^2 \tag{14}$$

then θ is related to R by[15]

$$\theta(\omega_0) = \frac{1}{2\pi}\int_0^\infty \frac{1}{R}\frac{dR}{d\omega} \ln\left|\frac{\omega + \omega_0}{\omega - \omega_0}\right| d\omega. \tag{15}$$

Let us transform this to wavelength and define

$$Y(\lambda) = \frac{1}{R}\frac{dR}{d\lambda} \tag{16}$$

for convenience

$$\theta(\lambda_0) = \frac{1}{2\pi}\int_0^\infty Y(\lambda) \ln\left|\frac{\lambda + \lambda_0}{\lambda - \lambda_0}\right| d\lambda. \tag{17}$$

We have measurements of Y only over a limited range of wavelengths. Therefore, to calculate θ we break the integral up into four regions with the following approximations:[16]

Region I: x-rays $0 \leq \lambda < \lambda_x$

In this region approximate $R \sim 1/\omega^A$ where A is an adjustable parameter.

Region II: vacuum ultraviolet $\lambda_x < \lambda < \lambda_1$

In this region use R measurements made by other experiments.

Region III: near infrared to near ultraviolet $\lambda_1 < \lambda < \lambda_2$

This is the region in which wavelength modulation data are available.

Region IV: far infrared $\lambda_2 < \lambda$

Approximate R by $R \sim e^{\alpha/\lambda}$.

With these approximations, the integral in Eq. (17) may be worked out for λ_0 in region III. After straightforward, though long, calculation, the result for $\theta(\lambda_0)$ is

$$\theta(\lambda_0) = -\frac{1}{2\pi}\left\{\int_0^\infty (Y(\lambda) - Y(\lambda_0))\ln\left|\frac{\lambda+\lambda_0}{\lambda-\lambda_0}\right| d\lambda + 2\lambda_0\int_{\lambda_1}^{\lambda_2} \ln R\,\frac{d\lambda}{\lambda^2-\lambda_0^2}\right.$$
$$+ \ln R(\lambda_1)\ln\left|\frac{\lambda_0+\lambda_1}{\lambda_0-\lambda_1}\right| - \ln R(\lambda_x)\ln\left|\frac{\lambda_x+\lambda_0}{\lambda_x-\lambda_0}\right| + Y(\lambda_0)\lambda_0\ln\left|\frac{\lambda_2^2-\lambda_0^2}{\lambda_0^2-\lambda_1^2}\right|$$
$$+ Y(\lambda_0)\lambda_2\ln\left|\frac{\lambda_2+\lambda_0}{\lambda_2-\lambda_0}\right| - Y(\lambda_0)\lambda_1\ln\left|\frac{\lambda_0+\lambda_1}{\lambda_0-\lambda_1}\right| + 2A\sum_{n=0}^{\infty}\left(\frac{\lambda_x}{\lambda_0}\right)^{2n+1}$$
$$\left.\times\frac{1}{(2n+1)^2} - \frac{\alpha}{\lambda_2}\ln\left|\frac{\lambda_2+\lambda_0}{\lambda_2-\lambda_0}\right| - \frac{\alpha}{\lambda_0}\ln\left|\frac{\lambda_2^2-\lambda_0^2}{\lambda_2^2}\right|\right\}. \qquad (18)$$

Each of these terms can be easily evaluated by a computor. By using re-

flectivity data from other experiments to extend the region II integral into the vacuum ultraviolet, results insensitive to the choice of the parameter A can be obtained.

The parameter α used in region IV is usually small because there are usually few electronic transitions in the infrared and they usually have little oscillator strength. Region I, which goes from the vacuum ultraviolet to higher energies, has more electronic transitions and more oscillator strength. Therefore, the A parameter is much more important than α, and the use of reflectivity data from other sources in region II is also important. A Kramers-Krönig analysis of only the lead salts was done because vacuum ultraviolet data was only available for these compounds we have investigated.

Once $\theta(\lambda)$ has been calculated from Eq. (18), the real and imaginary parts of the index of refraction can be calculated by

$$n = \frac{1 - R}{1 + R - 2\sqrt{R}\cos\theta} \tag{19}$$

$$k = \frac{\tan\theta(R + nR + n - 1)}{1 - R} \tag{20}$$

and ϵ can be calculated by

$$\epsilon_1 = n^2 - k^2 \tag{21}$$

$$\epsilon_2 = 2nk. \tag{22}$$

It is also possible to caculate $\frac{d\epsilon}{d\lambda}$ from the same data as used to calculate ϵ. By differentiating Eq. (17) we find

$$\frac{d\theta}{d\lambda}(\lambda_0) = \frac{1}{\pi}\int_0^\infty Y(\lambda)\,\frac{\lambda}{\lambda^2 - \lambda_0^2}\,d\lambda. \tag{23}$$

Again we break this integral up into four regions and make the same approximations for each region. The result is

$$\begin{aligned}\frac{d\theta}{d\lambda}(\lambda_0) = \frac{1}{\pi}\Bigg\{&\int_{\lambda_1}^{\lambda_2}(Y(\lambda) - Y(\lambda_0))\,\frac{\lambda}{\lambda^2 - \lambda_0^2}\,d\lambda + \int_{\lambda_x}^{\lambda_1}\ell nR\,\frac{\left(\lambda^2 + \lambda_0^2\right)}{\left(\lambda^2 - \lambda_0^2\right)^2}\,d\lambda \\ &+ \ell nR(\lambda_1)\,\frac{\lambda_1}{\lambda_0^2 - \lambda_1^2} - \ell nR(\lambda_x)\,\frac{\lambda_x}{\lambda_0^2 - \lambda_x^2} + \frac{Y(\lambda_0)}{2}\,\ell n\left(\frac{\lambda_2^2 - \lambda_0^2}{\lambda_0^2 - \lambda_1^2}\right) \\ &- \frac{A}{2}\,\ell n\left(\frac{\lambda_0 + \lambda_x}{\lambda_0 - \lambda_x}\right) - \frac{\alpha}{2\lambda_0^2}\,\ell n\left(\frac{\lambda_2^2}{\lambda_2^2 - \lambda_0^2}\right)\Bigg\}.\end{aligned} \tag{24}$$

By differentiating Eqs. (19) and (20) we find

$$\frac{dn}{d\lambda} = \frac{-Y(R + nR - n\sqrt{R}\cos\theta) - 2n\sqrt{R}\sin\theta\,\frac{d\theta}{d\lambda}}{1 + R - 2\sqrt{R}\cos\theta} \tag{25}$$

$$\begin{aligned}\frac{dk}{d\lambda} = &\left\{\frac{k}{\sin\theta\cos\theta} + \frac{2(\tan\theta - k)\sqrt{R}\sin\theta}{(1 + R - 2\sqrt{R}\cos\theta)}\right\}\frac{d\theta}{d\lambda} \\ &+ \frac{(k\sqrt{R}\cos\theta - kR - \sqrt{R}\sin\theta)}{(1 + R - 2\sqrt{R}\cos\theta)}\,Y.\end{aligned} \tag{26}$$

Calculation of $\frac{d\epsilon}{d\lambda}$ then follows quite simply. The same sensitivity to the parameters A and α is found here.

III. NOISE

To calculate the signal-to-noise ratio in wavelength modulation spectroscopy, let us look at the signal input into the signal lock-in amplifier. For simplicity, I will assume that the system is connected to measure $\frac{dR}{d\lambda}$. From Eq. (10) we have

$$S = I\Delta R + R\Delta I + AIR \tag{27}$$

where

$$A = -\frac{1}{c}\langle\Delta I\rangle \text{ and } c \approx \langle I\rangle. \tag{28}$$

The averaging of the reference signals to give A and c is done by the two feedback loops. The noise of the signal will be

$$\sigma_S^2 = \langle S^2\rangle - \langle S\rangle = R^2\sigma_{\Delta I}^2 \tag{29}$$

where $\sigma_{\Delta I}^2$ is the noise in the derivative of the reference intensity. We can estimate $\sigma_{\Delta I}^2$ by assuming that ΔI is the difference in two measurements of I at wavelengths of λ and $\lambda + \Delta\lambda$. Then

$$\sigma_{\Delta I}^2 = \frac{2\sigma_I^2}{(\Delta\lambda)^2} \approx \frac{2c}{(\Delta\lambda)^2} \tag{30}$$

assuming that the reference intensity obeys Gaussian statistics. Therefore, the signal-to-noise ratio of wavelength modulation spectroscopy is

$$\frac{S}{\sigma_S} = \sqrt{\frac{c}{2}} \frac{\Delta R}{R} \Delta\lambda. \tag{31}$$

It is possible to do derivative measurements by making accurate measurements of $I(\lambda)R(\lambda)$ and $I(\lambda)$ and then numerically calculating the derivative on a digital computor. The signal in this case is

$$S_D = \frac{\langle I(\lambda + \Delta\lambda)R(\lambda + \Delta\lambda)\rangle}{\langle I(\lambda + \Delta\lambda)\rangle} - \frac{\langle I(\lambda)R(\lambda)\rangle}{\langle I(\lambda)\rangle}. \tag{32}$$

Each term in averaging brackets <> represents an independent measurement. The noise in such an experiment will be

$$\sigma_D^2 = \sum_{x=1}^{4} \left(\frac{\partial S_D}{\partial x}\right)^2 \sigma_x^2 \tag{33}$$

where x runs over the 4 separate measurements. Again assuming Gaussian statistics

$$\sigma_D^2 = \frac{2R(1 + R)}{c} \tag{34}$$

and the signal-to-noise ratio is

$$\frac{S_D}{\sigma_D} = \sqrt{\frac{c}{2}} \frac{\Delta R}{\sqrt{R(1 + R)}}. \tag{35}$$

Since $R \sim \frac{1}{2}$, $\sqrt{R(1 + R)}$ is not going to be different from R by more than a factor of 2 or 3. Therefore, the signal-to-noise ratio for wavelength modulation spectroscopy and for digital computing techniques will be different by a factor of $\Delta\lambda$. In wavelength modulation spectroscopy, the signal-to-noise ratio can be improved by increasing the modulation ampli-

tude. This, of course, is done at the expense of optical resolution.

Several considerations have been left out of this discussion. When a photomultiplier is used with a lock-in amplifier, the "shot" noise effect of photoelectron pulses will contribute noise at the measurement frequency. The frequency spectrum of a short photoelectron pulse will look like white noise at the low measurement frequency. The "shot" noise power spectrum from pulses of width T is[17]

$$\sigma^2(\omega) = \frac{cT}{\pi(1 + \omega^2 T^2)} \tag{36}$$

where c is the average noumber of photons/second. The effective bandwidth of the lock-in is

$$\Delta\omega = \frac{2\pi}{\sqrt{8}\,\tau}$$

where τ is the output time constant. Therefore, the limiting rms value of the noise is

$$\sigma = \sqrt{\frac{2Tc}{\sqrt{8}\,\tau}} \sim 10^{-5}\sqrt{c} \tag{37}$$

for $T \approx 10^{-8}$ sec and $\tau \approx 10$ sec. For this reason, all modulation experiments are limited by the same "shot" noise effect to a resolution of 10^{-5}.

To achieve comparable resolution by numerical differentiation, the measuring equipment would have to be stable and precise to 10 ppm. Of course, the digital electronics would have to have a resolution of 10^5 or about 18 bits.

IV. EXPERIMENTAL RESULTS

A. Lead Chalcogenides

The three lead chalcogenides PbTc, PbSe, and PbS form semiconducting crystals in the rock salt crystal structure (space group Fm3m). Because of their small energy gaps they have been of interest for use as infrared detectors. Wavelength modulation measurements of reflectivity, $R(\omega)$, and logarithmic reflectivity, $(1/R)dR/d\omega$, have been made on all three compounds at temperatures between 5° K and room temperature. All of the samples used were cleaved single crystals. The crystals of PbTe and PbSe were small and did not cleave very well. Therefore, the magnitude of the reflectivity measured is not correct, although the relative values are still accurate. The results of the measurements at 5° K are shown in Figs. 7, 8, and 9. An empirical pseudopotential calculation was done at the same time by Y. Tsang and M. L. Cohen.[18] Their calculation of the logarithmic derivative of the reflectivity is also shown in Figs. 7, 8, and 9. The structures in all three spectra are very similar. Table I lists the peaks in the reflectivity measurements and critical points determined by the structure in $d\epsilon_2/d\omega$. The labelling E_1, E_2, etc. follows the notation of Cardona and Greenaway.[19] Also listed are the critical points calculated by Tsang and Cohen and their assignment to transitions in the Brillouin zone. For comparison, results from reflectivity,[19] absorption,[20] and electroreflectance[21] measurements are also included in this table.

It is possible for structure in $(1/R)dR/d\omega$ to originate from structure in $\epsilon_1(\omega)$ rather than $\epsilon_2(\omega)$. Aspnes and Cardona[21] showed that, in electroreflectance, $\Delta R \propto -\Delta\epsilon_1$ around the E_2 peak for all three lead

salts. An examination of the ϵ_1 and ϵ_2 spectra calculated from the WMS data confirms this result.

In measuring the reflectivity spectrum of PbS as a function of temperature, there is a pronounced sharpening in the fine structure at 5.08 eV as the temperature is decreased. This sharpening is observable even between liquid nitrogen and liquid helium temperatures. This is shown in Fig. 12. No other structure in the spectra of all three compounds has a similar behavior. The sample used in this measurement was n type with a carrier concentration of $\sim 10^{16}/cm^3$ as obtained from Hall effect measurements. However, when the measurements were repeated on an n type sample with a carrier concentration of $\sim 10^{18}/cm^3$, exactly the same spectrum is obtained as for the other sample, except for the 5.08 eV structure. In the sample with higher carrier concentration, the 5.08 eV structure is less pronounced at low temperature and does not show appreciable change from 5° K to 80° K. This result is similar to what is observed for the E_1 peak of Ge,[22] indicating that this structure is not simply due to band transitions. The strong temperature dependence and the dependence on carrier concentration seems to suggest that the structure may be due to excitonic effects. According to Table I(c), the E_3 peak is due to M_1 and M_2 critical point transitions at Σ and Δ. Based on the Toyozawa model,[23] hyperbolic excitons can therefore exist at the E_3 structure. One could argue that the high dielectric constant of PbS would prevent excitons in PbS. It is possible that excitons involving electrons in high conduction bands may see a smaller effective dielectric constant than even the high frequency dielectric constant ϵ_∞. The free carriers tend to screen the attractive interaction between electrons and holes, and this would explain why the excitonic effects decreases with

higher carrier concentration.

B. $ZnGeP_2$

The progression of the study of semiconductors, as noted in the introduction, has gone from the study of group IV semiconductors to the study of group III-V compounds. Structurally, the zincblende group III-V compounds can be obtained from the group IV diamond structures by replacing half of the group IV atoms by group III atoms and the other half by group V atoms in a systematic manner. When analyzing the electronic properties of group III-V compounds, the crystal potential (or pseudopotential) can be divided into a symmetric and an anti-symmetric part. The symmetric part can be approximated by the potential for the corresponding group IV element.

An extension of this trend is to look at the change in going from III-V compounds to ternary chalcopyrites with chemical formula ABC_2 where A is a group I or II atom, B is a group IV or III atom, and C is a group V atom. To go from a zincblende to a chalcopyrite, start with two unit cells of $D^{III}C^{V}$ stacked one on top of the other. Then, replace one half of the D atoms by A and the other half of the D atoms by B. The final crystal structure of the chalcopyrite is obtained by applying a small compression along the axis of the stacked unit cells. A schematic of the crystal structure is given in Fig. 13.

We have studied the chalcopyrite $ZnGeP_2$. The III-V analogue of this compound is GaP. The sample of $ZnGeP_2$ was a large single crystal obtained from Rochwell International Corp. The crystal was cut parallel to the {100} face. It was then mechanically polished and etched with "Syton." This produced a flat surface with a bluish-metallic appearance. The ex-

perimental (1/R)dR/dω spectra at 5° K are presented in Fig. 14 for light polarized parallel and perpendicular to the C axis of the crystal. For comparison, the modulation spectrum of GaP,[25] the III-V analog of ZnGe P_2, is also presented. The reflectivity at 5° K and at 300° K for both polarizations is shown in Fig. 15. As can be seen, the reflectivity spectra are dominated by two main peaks around 3.0 and 4.7 eV and a weaker structure around 3.7 eV. Following the notation of Stokowski[26] for several other II-IV-VI_2 compounds, the two main structures are labelled E_1 and E_2 and the weaker structure E_c. The E_1 and E_2 peaks are composed of several subsidiary structures. Table II lists the observed structures. A pseudopotential band structure calculation was done by C. Vera de Alvarez and M. L. Cohen.[27] The theoretical critical points calculated by them is also shown in Table II along with the assignment of critical points to transitions in the Brillouin zone. There is a general overall shift of 0.3 eV between theory and experiment which probably could be resolved by better choice of pseudopotential form factors. The measured and calculated reflectivities are shown together in Fig. 16 along with the labelling notation.

In doing a band structure calculation, the potential is usually written as a sum of atomic potentials. For $ZnGeP_2$, this can then be rearranged to give the following approximate potential[27]

$$V = V_{Zb} + V_A + V_\sigma. \tag{38}$$

V_{Zb} is the potential for the zincblende analog of $ZnGeP_2$. V_A is an anistropic term equal to the difference between the Zn and the Ge potential. V_σ is a potential produced because the crystal structure is distorted

from the "ideal" stacking of two zincblende unit cells. V_σ is equal to the potential of P times a structure factor of

$$\sum_{i=1}^{4} e^{i\vec{\beta}_i\vec{G}}\left(e^{i\vec{\sigma}_i\cdot\vec{G}_i} - 1\right) \tag{39}$$

where $\vec{\beta}_i$ are the position vectors of the P atoms in the "ideal" crystal structure, $\vec{\sigma}_i$ are the distortion vectors and $\vec{G}$ are the reciprocal lattice vectors. Since $\vec{\sigma}_i$ are small ($|\vec{\sigma}_i| \sim .1a$, a is the "ideal" cell side), this structure factor is going to be small for small $\vec{G}$. Since the pseudopotential for P (or any other element) is large for small G and small for large G, then V_σ is going to be a small perturbation on the "ideal" potential.

If we want to understand the spectrum of $ZnGeP_2$, we can start with the spectrum of GaP. Since V_{Zb} is the largest term of the potential, the coarse structure of the $ZnGeP_2$ spectrum is the same as the spectrum of GaP. However, the first Brillouin zone of the chalcopyrite is one-fourth the volume of the Brillouin zone of zincblende. If we ignore the distortions from the "ideal" structure, then the chalcopyrite Brillouin zone can be obtained by folding the zincblende zone using four different reciprocal lattice vectors. The potential V_A and V_σ will mix these four zincblende states to give more structure to the optical properties of the chalcopyrite. However, the structure factor for V_A is zero for two of the four folding reciprocal lattice vectors.[27]

The first optical transitions in $ZnGeP_2$ are transitions from the top of the valence band to the bottom of the conduction band at Γ. The Γ_{15} valence band in GaP is split by the crystal field splitting Δ_{CR} into a doubly degenerate band of Γ_5 symmetry and a single band of Γ_4 symmetry.

With the addition of the spin-orbit interactions, the Γ_5 state splits into states of $\Gamma_{\frac{7}{2}}$ and $\Gamma_{\frac{5}{2}}$ symmetry. The first optical transitions with significant oscillator strength are from the three valence band states to a conduction band of $\Gamma_{\frac{7}{2}}$ symmetry which is the analog of the Γ_1 state in GaP. These transitions, labelled A, B, and C have been seen and discussed by Shay[29] and Shileika.[28] In room temperature electroreflectance, Shay observes these transitions at 2.34 eV, 2.40 eV, and 2.48 eV, respectively. Shileika reports values of 2.46 eV, 2.53 eV, and 2.59 eV also from room temperature electroreflectance. At 5° K, I observe structures at 2.51 eV, 2.63 eV, and 2.67 eV. Using these values in the quasi-cubic theory of Hopfield,[30] the calculated spin-orbit splitting is Δ_{SO} = 0.13 and the crystal field splitting is Δ_{CR} = - 0.04.

The zincblende analog of $ZnGeP_2$ is an indirect gap $\Gamma_{15} - X_1$ semiconductor. When the Brillouin zone of GaP is folded into the Brillouin zone of $ZnGeP_2$, the X_1 states of GaP map into Γ states of $ZnGeP_2$. Furthermore, the effect of $V_A + V_\sigma$ is expected to be small near the band edge because the structure factors of V_A for the folded X states are zero and the structure factors for V_σ are small. Thus it is expected that the lowest interband transitions in $ZnGeP_2$ will have a very small oscillator strength, and $ZnGeP_2$ is referred to as a "pseudodirect" gap semiconductor. This has been observed for $ZnGeP_2$. Shileika[28] observes very weak transitions at 2.14 eV and 2.21 eV, labelled B' and C', in wavelength modulated absorption at 77 K. These are assigned to transitions from the spin-orbit split Γ_5 valence band to the Γ_3 conduction band. He also observes the band gap at 2.08 eV. In electroreflectance, Shileika observes very weak structure at 2.3 eV which are assigned to transitions $\Gamma_5 - \Gamma_2$, the analog of the $\Gamma_{15} - X_3$ transition in GaP. Shay[29] observes the B' and C' at

2.05 eV and 2.11 eV. In the present measurements at 5° K, a small structure is observed at 2.14 eV in both polarizations which agrees well with the results of Shileika. Weak structures are also observed at 2.29 eV for the perpendicular polarization and 2.31 eV for the parallel polarization. There are assigned to be the B" and C" transitions seen by Shileika.

As shown in Fig. 14, the experimental modulation reflectivity of $ZnGeP_2$ shows much richer structure than the modulated reflectivity of GaP. In the E_1 region corresponding to the two spin-orbit split peaks E_1 and $E_1 + \Delta_1$ of GaP, $ZnGeP_2$ has five resolvable structures. In general, these splittings are observed in most of the chalcopyrites studied so far.[31] Following the notation of Stokowski,[26] these five structures are labelled $E_1(1)$, $E_1(2)$, $E_1(3)$, $E_1(4)$, and E_c. The most important feature of these structures is the following: the energy separations $E_1(2) - E_1(1)$ and $E_1(4) - E_1(3)$ are close to each other for most of the chalcopyrites studied. This seems to indicate that the first transitions in the E_1 region are from two spin-orbit split doublets in the same region of the Brillouin zone. Both the experimental results for $ZnGeP_2$ and the results of the empirical pseudopotential calculation[27] show that this is not the case. The experimental splittings are 0.06 eV for $E_1(2) - E_1(1)$ and 0.21 eV for $E_1(4) - E_1(3)$. The results of the EPM calculation[27] show that the $E_1(1)$ and $E_1(2)$ peaks come from transitions in the N plane along the $2\pi(x1a, x1a, x1c)$ direction with $x \approx 0.2$. This is equivalent to the Δ transitions in GaP.

In the region of the $E_1(3)$ and $E_1(4)$ peaks of the experimental reflectivity, the EPM calculation finds two pieces of structure mostly in the perpendicular polarization. These two structures are found to come

mainly from transitions in the N plane of the Brillouin zone. One critical point is close to (0.3, 0.3, 0.38) and the other is close to (0.25, 0.25, 0). These two critical points have the same origin in the folded zincblende Brillouin zone. The lines (0, 0, 0) to (½, ½, Z) and (1, 0, 1) to (½, -½, Z-1) of the zincblende Brillouin zone when folded into the chalcopyrite Brillouin zone will cross in the first conduction band along a line close to the (¼, ¼, 0) to (½, ½, ½) direction. The interaction between these lines gives rise to the $E_1(3)$ and $E_1(4)$ peaks.

The E_c structure is associated with transitions at the X point. It is stronger in the parallel polarization. Care must be taken here because the theoretical[27] critical point is an M_0 critical point and the actual peak in the reflectivity is shifted about 0.1 eV to higher energy.

At higher energies, in the region corresponding to the E_2 peak of the reflectivity structure of GaP, at least five structures are observed. In the modulated reflectivity of $ZnGeP_2$, six prominent structures have been identified. The EPM[27] calculation shows that most of the contribution to the E_2 structure comes from transitions in the Δ and Σ directions of GaP, as expected. The Δ direction folds into the Δ, Λ, and (1-x, 0, 1) directions of the chalcopyrite Brillouin zone, while the Σ direction folds into the Σ, (x, 0 2x) and (1-x, 0, 2x-1) directions. Summation over k-space along the Δ and Σ directions shows that in effect the E_2 peak is mainly a Δ,Σ peak.

C. GaSe, GaS, and Their Alloys

The semiconducting III-VI compounds GaSe and GaS crystallize in layer structures. The arrangement of atoms within one layer is the same for both compounds. Within each layer the atoms form planes of atoms in a

VI-III-III-VI arrangement. Three different types of regular stacking of the layers have been described in the literature as β, ε, and γ modifications.[32] Large monocrystals of GaSe grown by the Bridgeman technique normally crystallize in a mixture of ε and γ modifications, whereas the stacking of GaS layers is invariably β type.[33]

GaSe and GaS form a continuous series of mixed crystals GaS_xSe_{1-x}. For $0.6 \leq x \leq 1$, the β modification predominates and the ε and γ modifications are found for $0 \leq x \leq 0.1$. In the intermediate region all three types of stacking are found.[33] Despite the fact that these crystals clearly exhibit two-dimensional structure and consequently have anisotropic mechanical properties, it has been argued that not all of the electronic states reflect this anisotropy. In particular, recent measurements of optical properties and of electronic transport properties have indicated that GaSe has nearly isotropic states in the forbidden band gap.[34]

All the samples used in this experiment were cleaved in the plane of the layers from large single crystal ingots. The single crystals were grown by the Bridgeman technique in sealed quartz ampules. The starting material consisted of an admixture of pure (99.9999%) polycrystalline GaSe and GaS. Except for the top and end of the ingot, no noticeable variations of composition has been found for crystals grown under appropriate conditions. The composition of the crystal alloys was measured by an x-ray fluorescence technique. The samples were homogenous to within 1%. Unless otherwise stated, all measurements were made at 5° K. Measurements were with unpolarized light incident almost parallel to the C axis.

In Fig. 17, the measured reflectivity of GaSe is presented. Also,

a pseudopotential band structure calculation was performed by M. Schlüter.[35] The calculated reflectivity is also presented in Fig. 17. This derivative reflectivity of GaSe is presented in Fig. 18 along with the calculated derivative reflectivity. The calculated reflectivity had to be shifted 0.4 eV to higher energy to achieve satisfactory agreement with experiment. Since all important transitions below 5.5 eV terminate at the first conduction band pair (bands 19 and 20), the shift in the reflectivity curve can easily be obtained by rigidly shifting the main portions of bands 19 and 20 upwards.

Although the experiment was performed in the E $\perp$ c polarization, the angle of incidence of the light beam ($\sim 5°$) and the finite solid angle of the beam ($\sim 5°$ aperture) allow the presence of E $\parallel$ c polarization. Due to this E $\parallel$ c component which is combined with a strong matrix element anisotropy,[36] the experimental spectra are best compared to theoretical spectra calculated for unpolarized light. The precise positions of structure in the measured and calculated reflectivity are obtained from the respective derivative spectra (Fig. 18). Their energy values together with their band structure assignment are given in Table III. The notation for labelling the structures will be described below.

One particular structure, S1, on the rising shoulder of the first peak (GS2) is of particular interest. According to the band structure calculation,[35] the structure observed around 3.4 eV is identified with the transition $\Gamma_5^- - \Gamma_3^+$. The transition is very Se like, i.e. its initial state is predominately Se p_x and p_y character and the final state shows appreciable Se s-admixture. Since its first observation in absorption by Subashiev et al.,[37] the S1 transition has been extensively studied and assigned to i) a saddle point excition,[38-39] to ii) an M_1 critical

point[40-41] or to iii) an excitonic transition at an M_0 critical point.[42-43] To emphasize the excitonic character of the transiton S1, in Fig. 19 a comparison between a) the wavelength modulation spectrum at 300 K, b) the electroreflectance spectrum at 300 K, c) the reflectivity at 300 K and d) the reflectivity at 5 K. The electroreflectance measurements were done by the electrolytic method following Ref. 40 with similar results as Ref. 40.

The striking feature of the electroreflectance spectrum is that the most important response is at S1 and not at the main reflectivity peak GS2. This large electro-optic enhancement clearly confirms the excitonic nature of transition S1. On high quality single crystal samples, the reflectivity peak can be resolved into two components at low temperatures (Fig. 19d). They are attributed to the excitonic ground state and the continuum states. The observation of an n = 2 exciton state can be ruled out on the basis of oscillator strength and lifetime arguments. From these two structures, the exciton binding energy is $E_B = 30 \pm 5$ meV. Though the two structures can be clearly observed, their amplitude is too small to permit line-shape analysis. Using the values of $\varepsilon_{0\parallel} = 7.6$ and $\varepsilon_{0\perp} = 10.2$ for the static dielectric constant, the band masses for different types of excitons at S1 are compiled in Table IV.

The isotropic M_0 exciton model[44] leads to a reduced mass of $\mu = .17\ m_0$. The anistropy of the conduction band masses ($m_{c\parallel} = .3$ and $m_{c\perp} = .17$) has been measured by magneto-optic and transport methods.[34] Therefore, the isotropic M_0 exciton would require a very strong valence band mass anistropy of the opposite sign. The two-dimensional[45] and three-dimensional hyperbolic exciton[46] models both result in a transverse reduced mass $\mu_\perp = 0.06$. These can also be dismissed for similar reasons

to the isotropic exciton model.

The empirical pseudopotential calculation of Schlüter[35] indicates an anistropic M_0 critical point for the S1 transition. For a three-dimensional hyperbolic exciton model[47] the lower limit of $\mu_{\parallel}$ is 0.17 (the isotropic mass). If the valence band masses are assumed to be very large, then an anistropy parameter

$$\alpha = \frac{\mu_{\perp} \epsilon_{\perp}}{\mu_{\parallel} \epsilon_{\parallel}} = 0.76 \qquad (40)$$

leads to a binding energy of $E_B = 33$ meV, in excellent agreement with the measured value.

Both the reflectivity and the wavelength modulated reflectivity of GaS_xSe_{1-x} have been measured at about 5° K for a series of 10 mixed crystals. The composition x of GaS_xSe_{1-x} varies gradually by steps of about 1/10 from 0 to 1. The exact values of x dtermined by a microprobe technique are 0.10, 0.22, 0.31, 0.40, 0.47, 0.51, 0.57, 0.66, 0.72, 0.76, and 0.91. In Fig. 20 an illustration of the general variation of the reflectivity spectrum is given. Despite an increased broadening of the spectra for intermediate compositions, probably resulting from structural disorder and despite a weakening of some spectral structures, most of the assigned structures of GaSe (Table III) can be followed through the series to GaS.

The following general trends can be noted from Fig. 30 and Table III:

i) The main structures shift to higher energies for increasing sulphur concentration x.

ii) The low energy peak GS1, GS2 (at 3.8 eV in GaSe) narrows consider-

ably with increasing x resulting in a very sharp dominating structure in GaS.

iii) The characteristic two-peak structure of GaSe gradually transforms into a more complicated spectrum in GaS.

Detailed analysis of the spectral changes as a function of x reveals linear shifts for almost all important structures. Moreover, according to their shifts (Δ), these structures, including direct and indirect gap at about 2.0 eV,[48] can be grouped into three different classes with zero ($\Delta \approx 0$), intermediate ($\Delta \approx 320$-400 meV) and strong ($\Delta \approx 780$ meV) shifts, respectively. In the pseudopotential calculation of the band structure GaSe by Schlüter,[35] calculations of charge density contours and the optical transition function

$$F(\vec{r}) = \psi_i(\vec{r})\vec{p}\psi_f(\vec{r}) \tag{41}$$

were made. The volume integral of F is the optical transition dipole matrix element. This information was used to determine the degree and nature of the real space localization of optical transitions. Distinctions can be made between atomic-like (intra-ionic), charge-transfer-like (inter-ionic) or bond-like (bonding-antibonding) transitions. These are described in a), b), and c) below.

a) Transitions with strong cation (Ga) character and zero energy shift ($\Delta \approx 0$ meV).

Four main structures of Table III labelled G1 to G4 (G stands for predominant gallium character in the corresponding wavefunctions) belong to the $\Delta = 0$ class. Their energies which are displayed in Fig. 21 as a function of composition x show no overall shift if sulphur is substituted

for selenium. Experimentally G1 and G2 can easily be followed through the entire composition range whereas G3 and G4 are only resolved in crystals with higher sulphur concentration. For low values of x, G3 and G4 merge with the strong S_3, S_4 structure which dominates the spectrum in this energy range and cannot be resolved. In GaSe the structures G1, G2 are assigned to transitions between the topmost valence band and the bottom conduction band near the point H in the hexagonal Brillouin zone.[35] The two-fold degeneracy of the valence band at H is lifted by the inclusion of spin-orbit interaction. The resulting splitting which according to an analysis of the wavefunctions should result from Ga p-levels is most likely to be responsible for the double structure G1, G2. This assignment is strongly supported by the observation of a constant splitting of 0.12 eV between G1 and G2 throughout the entire alloy series. Moreover the observed value of 0.12 eV agrees well with the atomic Ga 3p spin-orbit splitting of about 0.09 eV.

In the charge density calculations of the initial and final states of the G1 and G2 transitions given by Ref. 35, the charge in both states is concentrated around the Ga cores and very little charge sits around the anions. This obviously explains the very small shift of the critical point energy with increasing sulphur concentration. The transitions G1 to G4 thus represent the particular case of pure cation transitions whose energy is at most slightly affected by anion-alloying. The existence of these transitions is caused by the particular crystal structure of GaSe and GaS in which like-atom bonds exist.

b) Transitions with mixed anion (S, Se)-cation (Ga) character and intermediate energy shifts (Δ = 320 to 400 meV).

In Fig. 22 the energies of several transitions (GS1 to GS6) are

displayed as a function of concentration x. The measured energy shifts can be fitted linearly with slopes varying between 320 and 400 meV. The structure labelled GS1 which corresponds to a small shoulder in the reflectivity cannot be observed for $x > 0.3$, not even in the wavelength modulated spectrum. GS2 corresponds to the main structure found in the reflectivity of GaSe at 3.8 eV. The shift of this structure is found to be linear with concentration for $x > 0.2$. For $x > 0.3$ the two structures GS2 and GS3 overlap resulting in a broad peak with little resolved fine structure. The possibility of connecting GS1 and GS3 by a discontinuity of 200 meV at about $x = 0.3$ similar to the observed 50 meV step of direct and indirect gap[48] due to changes in the stacking sequence cannot be ruled out inspite of the large energy difference. As seen in Fig. 20 the shape of the GS2, GS3 structures changes drastically between GaSe and GaS. The peaks narrow considerably with increasing sulphur concentration and become the predominant features of the reflectivity spectrum for $x > 0.5$. The splitting between GS2 and GS3 which is not resolved for $x < 0.3$ has a value of 0.17 eV in GaS.

According to the assignment in GaSe the transitions take place between the topmost valence bands and the lowest conduction bands along the lines T, S and their connecting line in k-space[35]. Interlayer interaction is not likely to cause the GS2, GS3 splitting because of the very different oscillator strength of the transitions in GaS. In fact, the line shape of the strong GS2 peak in GaS is reminiscent of the asymmetric singularity associated with a two-dimensional M_0 critical point (c.p.) excitonic transition.[9] Indeed a comparative inspection of the GaSe band structure lends some support to the existence of a two-dimensional M_0 c.p. for GaS in the T, S region of k-space. On the other hand

no excitonic character would be needed to explain the GS2 line shape if one assumes a nearly degenerate pair of two-dimensional $M_0 + M_1$ c.p.'s. The observed strong temperature dependence of the GS2 peak is compatible with both models. The likelihood of the observation of a two-dimensional M_0 c.p. exciton followed by the c.p. band edge for the GS2, GS3 structures in GaS in illustrated in Fig. 23. Since the real part of the refractive index dominates the imaginary part by a factor of about 10 in this energy range,[42] the reflectivity can be calculated from the functional behavior of $\varepsilon_1(\omega)$ alone. The fit of the reflectivity in Fig. 23 is obtained with a background dielectric constant of $\varepsilon_1 = 7$, a band edge transition energy of $E_0 = 4.195$ and an exciton binding energy of 170 meV. No additional life-time broadening is included and an oscillator strength of unity for both the exciton and the band edge transition is used. The exciton binding energy of 170 meV leads to a reasonable transverse reduced bass mass of $\mu_\perp = 0.15$. More experimental evidence as to the nature of the GS2, GS3 transition in GaS, however, has to be presented, before conclusive answers can be given. In particular, electroreflectance measurements as carried out on the 3.4 eV structure (S1) of GaSe should certainly be helpful in answering the question about the existence of excitonic character in the GS2 transition. However, our experiments along these lines on GaS were unsuccessful.

The pseudopotential calculation of Schlüter[35] assigns the GS transitions along the lines T and S between zone center, Γ, and the zone boundaries at H and K. The charge density distribution show these transitions to be of mixed cation and anion in character. The amount of anion admixture is smallest at H and increases along the lines T and S reaching a maximum at Γ. The calculation shows that most of the energy

shift Δ seems to originate from a valence band shift which contains variable amounds of Se p_z-like character.

c) Transitions with predominant anion (S, Se) character and strong energy shifts (Δ = 780 meV).

Four main transitions S1 to S4 which exhibit a large energy shift Δ ≈ 780 meV are shown in Fig. 24. The high energy doublet S3-S4 observed at 4.86 and 5.13 eV in GaSe can be followed through the alloy series up to 5.57 eV and 5.78 eV respectively in GaS. The structure S2 is weakly seen in GaSe but it becomes important in GaS where it merges with the GS4 line. The low-energy structure S1 corresponds in GaSe to the anisotropic three-dimensional M_0 c.p. exciton which has been discussed at length above. It shifts linearly to higher energy with increasing sulphur concentration and disappears at x ≈ 0.3, 0.4. No equivalent structure can be observed in GaS at the extrapolated energy range. The same difficulty has previously been reported in absorption measurements carried out at 90° K.[49] Our modulation measurements, however, show a pronounced doublet at 4.55 and 4.61 eV in GaS, very similar to the S1 doublet observed at 5° K in GaSe. The similarity of the line shapes is explicitly shown in Fig. 25. It is suggestive that these similar structures can be assigned to the same transition since they exhibit identical energy shifts and both disappear at a composition range of x ≈ 0.3, 0.4. The doublet splitting in GaS is about 60 meV, twice the splitting observed for GaSe. This difference can reasonably be explained by different exciton binding energies. The sudden changes in transition energies at x ≈ 0.3, 0.4 is presumably due to the structural transition from γ,ε to β type stacking reported in this composition range.[48] This structural transition has also been found to be responsible for a 50 meV step in both direct and

indirect gap energies[48] and for the intensity drop-off of the 135 cm^{-1} Raman mode associated with the β-polytype. In the case of the S1 transition the step is about 400 meV which would indicate a high sensitivity to stacking sequences of the states involved.

For the S1 transition, the final state, which is at Γ in the first conduction band pair, has partially antibonding Ga-Ga character combined with strong Se s, p_z-type character. This explains the sensitivity of the Γ-state to anion alloying. Moreover, the initial state exhibits exclusively Se p_{xy}-character and therefore is also strongly affected by alloying. The corresponding transition is strongly localized on the anion site and corresponds mainly to an Se p_{xy} to s atomic-like transition.

The direct gap at Γ at ~ 2 eV also shows the strong experimental shift $\Delta \approx 780$ meV if selenium is substituted by sulphur.[48] The Γ state of the top valence band has in addition to Ga-Ga bonding character, a strong, nearly pure Se p_z-like character. It is therefore also sensitive to anion alloying. The direct gap transition corresponds partially to the excitation of the Ga-Ga bond. However, as seen from the transition function in Fig. 15, considerable contributions originate from anion p_z to s atomic-like transitions. This has not been emphasized before. It is clearly responsible for the large energy shift Δ of the direct gap.

D. SnS_2 and $SnSe_2$

SnS_2 and $SnSe_2$ crystallize in a hexagonal closed packed CdI_2-type structure. Within one layer, a plane of metal atoms is sandwiched between two planes of chalcogenides such that each metal atom is octahedrally surrounded by six chalcogen atoms. From optical absorption measurements,[50-54] the fundamental absorption has been found to be indirect

in both compounds and forbidden for polarization perpendicular to the C axis. The band edge energies are about 2 eV for SnS_2 and 1 eV for $SnSe_2$. In the range of interband reflectivity spectra, very little work has been done: i) room temperature relectivity[50] has been reported for SnS_2 in the range 1 eV to 12 eV and, ii) room temperature and liquid nitrogen temperature reflectivity[55] have been reported for $SnSe_2$ in the range 1.5-5 eV. The reproducibility of the results in this case, obtained on different samples, is somewhat questionable.

All samples used were grown by iodine transport technique. As usual, the samples were flat with their large surface ($\sim 1\ cm^2$) perpendicular to the C axis. Their thickness was only a few tenth of a millimeter, which prevented any attempt to polish them and to perform measurements in the configuration $E \parallel C$. Consequently, these measurements are restricted to the standard configuration $E \perp C$. Due to the good quality of the natural faces, the crystals were used "as grown." No difference between the spectra obtained in these conditions and a spectrum obtained on a freshly cleaved face was found. Measurements on different sample crystals were reproducible.

Fig. 26 represents the experimental reflectivity spectra of SnS_2 at room temperature and at liquid helium temperature. As usual, the structures shift to higher energy and become much sharper when the temperature lowers. This is clearly seen on the differential reflectivity spectra of Fig. 27. As will be seen in more detail below, the structures in our reflectivity spectrum are mainly due to transitions from a group of six top valence bands to the lowest conduction band. Many fine structures appear at low temperature and correspond to transitions at specific critical points and lines in the Brillouin zone.

Around 2 eV, a rapid change in reflectivity appears in SnS_2 which is indicative of the absorption edge. However, it is difficult to believe that the strong structure seen in differential reflectivity in Fig. 27 is only due to indirect forbidden transitions;[50-51,53-54] one has probably in the same range of energy a close superposition of direct and indirect transitions. In Table V, we compare the indirect gap energies found in our derivative spectra with those reported in absorption measurements.

Fig. 28 displays the reflectivity spectra of $SnSe_2$ from 1.5 eV to 6 eV at 300° K and 5° K. The wavelength modulated spectra are given in Fig. 29. Comparison with the SnS_2 spectra shows the following:

i) There is a shift of the overall structure to lower energies by about 1 eV. This is reminiscent of the shift (0.8 eV) observed on GaS_xSe_{1-x} alloys for optical transitions with a large charge concentration on anion sites. Total charge density maps calculated by M Schlüter[56] suggest a similar situation for the present case.

ii) The large structure around 4 eV is considerably broader than in SnS_2 (4.9 eV) and displays many more fine structures. The lowest structure, seen around 2 eV in Fig. 28 correlates well with previously reported absorption data.[54] The fundamental absorption edge at 1.24 was out of our range of investigation.

The precise position of structures is obtained from the derivative spectra. We list them in Table VI for SnS_2 and in Table VII for $SnSe_2$ together with the results of previous investigations and their theoretical assignments in a empirical pseudopotential band structure calculation by Schlüter and Schlüter[57] and by Fong and Cohen.[58]

As already mentioned, SnS_2 (and also $SnSe_2$) is a material with a strong indirect gap whose energy has been reported in absorption at about

2.40 eV at 80° K.[50] EPM band structure calculations[57-58] on SnS_2 also reveal a strong indirect gap between the states Γ_2^- and M_1^+ at about 2.2 eV. Group theoretical arguments show that this indirect transition is forbidden for polarization $E \perp C$ which is in accord with experimental findings. Although the two band structures of Ref. 57 and 58 show reasonable overall agreement and also quantitative agreement in the immediate vicinity of the fundamental gap, they differ somewhat for higher energy optical transitions.

The first structure found in the differential reflectivity (Fig. 27) appears around 2.5 eV. The richness of structure suggests a close mixing of several direct and indirect transitions in the same range of energy. The situation is quite similar to an observation on $SnSe_2$[54] where three gaps, two indirect forbidden and one direct allowed, have been reported within 1 eV. An inspection of the band structure[57] further supports the suggestion.

The next set of structures found in differential reflectivity is located around 2.8 eV (2.61, 2.70, 2.81, 2.90, 2.95). It corresponds to a small structure seen in reflectivity around 3 eV and is attributed to some transitions between bands 8 and 9 (topmost valence band and lowest conduction band) around the the points M and L in the Brillouin zone. According to the theoretical results of Ref. 57 these transitions are direct and forbidden. Another set of weak, broad peaks in the reflectivity appears around 3.37 and 3.80 eV. The peak at higher energy is resolved into structures at 3.61, 3.80, and 3.92 eV in the differential reflectivity and corresponds to the structure previously reported at room temperature by Greenaway et al.[58] The room temperature measurements give the structure at 3.57 eV. According to the band structure, these transitions

take place along the line Σ between bands 8 and 9.

So far we were concerned with structure of relatively low intensity which is due either to small transition matrix elements (indirect transitions, forbidden transitions) or to small joint density-of-states contributions. In contrast to this, the next higher energy transitions correspond to the two strong maxima of reflectivity found at 4.98 eV and 5.85 eV at 5° K, displayed in Fig. 26. Around the lower peak, our differential reflectivity spectrum reveals at low temperature four structures which are seen as weak shoulders in the reflectivity. They are located at 4.17 eV and 4.53 eV on the low energy side and at 5.32 eV on the high energy side of the 4.98 eV peak. At room temperature the dominant structure is found at 4.89 eV. The second main peak in the reflectivity at higher energies (5.8 eV at 5° K) shows only one shoulder at its low energy side (5.58 eV) in the differential reflectivity.

As indicated in Table VI, the structures forming the main peak around 4.98 eV correspond to transitions which take place along the lines T and P, including the high symmetry points K and H between the topmost valence bands (they are degenerate along P) and the lowest conduction band. Inspection of the corresponding calculated charge density maps shows that these transitions excited electrons from sulphur P_z-like orbitals into sulphur and tin S- and P-like orbitals. In contrast to these transitions, the second big peak in the reflectivity at 5.85 eV corresponds to transitions in which electrons from sulphur P_{xy}-like orbitals are promoted into sulphur and tin S- and P-like orbitals. These transitions take place along the lines Σ (and S) between lower valence bands (6) and the first conduction band. The theoretical and experimental findings are summarized in Fig. 30 where a calculated reflectivity based

on the band structure of Ref. 57 and the measured reflectivity are compared. The strong disagreement in amplitude for the 4.98 eV structure is probably due to the existence of excitonic character of these transitions.[50]

We have investigated the temperature dependence of the differential reflectivity spectra (Fig. 31) and we found that most of the temperature dependence of the broadening parameter occurs between 100° K and 300° K. This supports a characteristic temperatrue of exciton-phonon interaction in SnS_2: $\theta \sim 100°$ K, which suggests a large reduced mass for the exciton.

We have seen that the dielectric response of SnS_2, up to about 6 eV, consists mainly of two peaks. Roughly speaking one can attribute these two main peaks to transitions from sulphur P-like states into sulphur and tin S- and P-like states. The splitting of about 0.9 eV between the two peaks is caused by the anisotropic crystal field splitting of the sulphur P-like levels. Similar splittings with the P_{xy}-like levels at lower energy than the P_z-like levels have also been found in other layer compounds like GaSe or GaS. These two main peaks originate from transitions which take place at locations in $\underset{\sim}{k}$-space which are close to "special $\underset{\sim}{k}$-points" as it has also been found for GaSe.

The interpretation of the $SnSe_2$ spectra results in similar conclusions as obtained for the SnS_2 spectra. Mainly there are two large peaks in the reflectivity between 2 and 6 eV which can roughly be assigned to transitions from the crystal-field split selenium P_z and P_{xy}-like levels to the selenium and tin S- and P-like levels. The difference from the SnS_2 spectra however is the appearance of more fine-structure and more spreading out of the first main peak, coupled to a decrease in intensity.

$SnSe_2$ has an indirect, forbidden band gap like SnS_2 around 1 eV (see

Table VII). The theoretical value is close to this value within 0.1 eV. A second indirect forbidden transition has been reported at about 0.3 eV higher energies.[54] Theoretically these transitions could correspond to final states between M and L in the Brillouin zone.

The first experimental structure found in our work is at 1.92 eV. This structure is clearly seen on the reflectivity spectra of Fig. 4 and agrees well in psoition with the first direct transition reported in absorption.[54] The peak, however, is broad which may indicate contributions from different points in the Brillouin zone. Even with first order differential spectroscopy it was not resolved accurately. Theoretically, the first direct (forbidden) transitions occur at about 1.7 eV between M_2^+ and M_1^+. The next structure about 2.0 eV is also seen in reflectivity, but not resolved in any previous work. Theoretically, these weak transitions occur between M and Γ in the Brillouin zone.

The first large structure is observed between 3.5 and 4.5 eV and obviously corresponds to the first main structure around 5.0 eV in SnS_2. In $SnSe_2$, however, this structure is broad and extends over about 1 eV and features up to five resolved transition peaks in reflectivity (3.6 eV, 3.75 eV, 3.9 eV, 4.2 eV, and 4.45 eV). Many fine structures are found in the modulated reflectivity spectrum and are compiled in Table VII together with the tentative theoretical assignments.

The experimental reflectivity spectrum is compared with a calculated spectrum based on the band structure of Ref. 58 in Fig. 32. Schlüter,[56] calculated the charge densities and optical transfer function for some of the electronic transitions. He showed that several of the electronic transitions are very localized in real space, just as was seen above for GaSe. In particular, the transition labelled Z1 is a transition between

an Se P_z-like orbital and Se S- and P-like orbitals. The valence band state wavefunction has clear P_z-like character. The Z1 transition has E ∥ C polarization dependence. In contrast, the M_{8-10} transition, which is also localized around the Se ion, has E ⊥ C polarization dependence. This is because the valence band state wavefunction has P_{xy}-like character.

E. HfS_2

Another example of a layer compound which crystalizes in the CdI_2 structure is HfS_2. In contrast to SnS_2 discussed above, Hf is a group IVB transition metal element. As will be seen, the optical properties of HfS_2 are quite different. The most striking feature is a reflectivity minimum of less than 2% at about 4 eV, above the first strong optical transition.

A number of previous measurements have been made on HfS_2. Absorption measurements[59] support an indirect energy gap of value 1.96 eV at room temperature and a temperature coefficient of -4.3×10^{-4} eV/K° in the range of 77-500° K. An independent electrical determination[60] gives a slightly higher value of 2.1 eV. At liquid helium temperature, transmission measurements performed on thin adhesive cleaved samples[61] have been able to resolve some fine structures in the range 2.5-3.5 eV.

Several band structure calculations of HfS_2 have been made in the past. Murray *et al.* (MBY)[62] used a semi-empirical tight-binding scheme with three empirical parameters. Mattheiss[63] applied the augmental plane wave method at a few important points in the BZ. The band structure along symmetry directions was then obtained by Slater-Koster's tight-binding interpolation scheme. Fong[64] has done a full empirical

pseudopotential band structure calculation.

The HfS_2 crystal used had a large face of 10 x 5 mm and a thickness of 10 μm. The thickness was deduced from the interference fringes shown in Fig. 33 around 2.2 eV. These fringes arise from interference between light reflected off the front and back surfaces of the sample when the incident photon energy is below the direct band gap of the sample. The C axis was perpendicular to the platelet. Because of the small sample thickness, measurements were restricted to the $\vec{E} \perp C$ polarization. A natural, "as grown", face of the platelet was used for measurements. The measured spectra showed some sensitivity to the position of the light beam on the sample surface. This was particularly true of structure at higher energies. Presumably this was associated with defects in the layer stacking.

In Fig. 33 the reflectivity, $R(\omega)$, and its logarithmic derivative were plotted as functions of photon energy, $\hbar\omega$. In general, the reflectivity shows prominent structures for $\hbar\omega \leq 3.5$ eV, a strong drop-off above 4.0 eV and a fairly constant "plateau" observed up to 6 eV. The minimum of the reflectivity at 4.23 eV is only about 2%. The magnitude of the reflectivity of the "plateau" is sensitive to the position of the focused beam on the sample surface. As usual, the derivative spectrum displays many fine structures.

The first prominent structure in our experimental reflectivity spectrum is at 2.83 eV. Compared to the value reported by Greenaway and Nitche[59] (2.9 eV) and the one given by Beal et al.[61] (2.8$_6$ eV), our peak is about 60 meV lower. This difference may be due (a) to the increased accuracy achieved in the modulation spectroscopy, and (b) to the shift of peak energies between absorption and reflectivity spectra. The

theoretical spectrum in this range shows a weak shoulder at 2.7 eV and a peak at 2.9 eV. Fong[64] assigns the peak to the observed structure at 2.83 eV. Both theoretical structures come from regions near Δ (line Γ → A) from transitions of the uppermost valence band to the lowest conduction band (8 → 9 transitions) except that the 2.7 eV contour does not enclose the point A. No correlation of this structure with the point L in the BZ, as suggested by MBY,[62] was found. Their calculated energies of transitions $L_2 \rightarrow L_1$ and $L_3 \rightarrow L_1$ (assigned by MBY as the direct gap) are at 3.47 and 3.6 eV, respectively. Hence, it will be impossible to account for the 2.83 eV experimental structure in a spectrum deduced from their band structure. The result of the APW calculation[63] suffers the same shortcoming, since the calculated minimum direct gap at 3.43 eV is also at L. From our calculation, we suggest that the fundamental direct gap of HfS_2 is at $\Gamma(\Gamma_2^- \rightarrow \Gamma_3^+)$ with a gap energy of 2.4 eV and rather weak dipole transition matrix elements, and the contribution to the 2.83 eV structure is due to the volume effect.

The two next structures around 2.94 and 2.99 eV in the derivative reflectivity spectrum agree with the ones at 3.03 and 3.07 eV in the transmission data.[61] The splitting in our case is 50 meV, and agrees with the value (~ 65 meV) calculated by MBY for the spin-orbit splitting of the Γ_3^- band.[6,7] However, the intergand energy of $\Gamma_3^- \rightarrow \Gamma_1^+$ given by MBY is 4.08 eV which is about 1 eV higher than the measured value of the structure. Beal et al.[61] identified the 3.07 eV shoulder as the transitions associated with $M_1^- \rightarrow M_1^+$, i.e. 8 → 9 at M. Our theoretical result shows a shoulder at 3.1 eV. It is not resolved into two structures since the resolution of the calculation is only 0.1 eV. The contributions to this structure are from 8 → 9 transitions near the L point

and 7, 8 → 11 transitions around the A point. Both regions have strong dipole matrix elements. Since part of the contributions associated with the degenerate valence bands at the point A ($A_3^- \rightarrow A_1^+$), it is possible that the 50 meV splitting is due to spin-orbit splitting of these degenerate bands.

The 3.2 eV structure in Refs. 59 and 61 is seen in our experimental spectrum (Fig. 33) as a shoulder at 3.17 eV with no splitting resolved. The transition possibly responsible for the structure is $L_2 \rightarrow L_1 (7 \rightarrow 9)$ but its contribution is not visible in the calculated spectrum as it is masked by the strong peak at 3.3 eV.

Both experimental and theoretical spectra show a strong peak at 3.3 eV, which presumably corresponds to the 3.23 eV peak in the absorption spectrum. This peak was identified in Ref. 62 as due to $\Gamma_3^- \rightarrow \Gamma_1^+$ transitions. Their calculated energy of this peak was however, at 4.08 eV. The calculation of Fong[64] finds that the peak comes from 8 → 9 transitions in an extended region very near the ΓALM plane in the BZ. A nearby critical point with M_1 symmetry is found along $R\left[\left(\frac{1}{3}, 0, \frac{1}{2}\right) \frac{\sqrt{2}\pi}{a}\right]$ at 3.25 eV. The strong dipole transition matrix elements near the plane enhance the intensity of the peak.

In the higher energy region, both spectra in Fig. 34 show a structure at 3.5 eV which can be attributed to the $M_1^- \rightarrow M_1^+$ (8 → 9) transitions. The theoretical spectrum has a structure at 3.9 eV which differs from the experimental structure at 3.8 eV by 0.1 eV and is due to the volume effect in two extended regions: (a) 8 → 9 transitions with cylindrical contour surface intersectiong the midpoints of the S and T lines and the zone boundaries near L and M; (b) 7 → 9 transitions with contour surface almost parallel to the AΓLM plane. The dipole matrix elements

associated with these transitions are weak. The peak at 4.4 eV is mainly due to the 7 → 9 transitions with contours similar to the one given in (b) except it is farther away from AΓLM planes.

A fast drop in the reflectivity around 4.1 eV is exhibited in both experimental and calculated spectra, although the one in the theoretical spectrum appears to be less drastic. A similar dip has been observed in Refs. 59 and 61. The calculation of Fong[64] shows that this is due to exhaustion of oscillator strength of the 8 → 9 and 7 → 9 transitions. The experimental reflectivity starts arising gradually after 4.2 eV and reaches a weak maximum at 4.9 eV. This is in good agreement with the result of Greenaway and Nitche.[61] The corresponding structure in the theoretical spectrum of Fong is 0.3 eV lower and the magnitude is about seven times higher. The main contribution to this peak comes from 7 → 10 transitions in the region near Δ but above the ΓMK plane. The discrepancy in the higher region has been found in many pseudopotential calculations of semiconductors. The above discussion is summarized in Table VIII.

F. SbSI

The semiconducting and ferroelectric crystal SbSI has many unusual properties. On cooling down from room temperature, SbSI undergoes several phase transitions.[65] The high temperature phase above 19° C is paraelectric; the low temperature phases are ferroelectric. SbSI has very strong anisotropic properties[66] related to the fiber-like nature of the crystal structure. It has the largest known piezoelectric constant and saturated polarization.[67] It has strong nonlinear optical properties.[68] The phase transition involves relatively large changes

in the crystal structure,[65] therefore it is plausible that changes in the reflectivity can be observed across the 19° C phase transition.

The SbSI crystal used had a dimension of about $10 \times 1 \times 1$ mm^3. The $\hat{c}$-axis and the [110] direction were respectively parallel and perpendicular to the rectangular faces. Optical measurements were made on one of these faces with light polarized parallel and perpendicular to the $\hat{c}$-axis. Unfortunately, we were not able to obtain a crystal with a sufficiently large surface parallel to either $\hat{a}$ or $\hat{b}$ axis.

The spectra of SbSI was measured at many different temperatures, in particular, near the phase transitions. No detectable change in the spectra was observed at the transitions. The spectra at 5° K and 300° K are shown in Fig. 35. At low temperature, the reflectivity with $\vec{E} \parallel \hat{c}$ has the main peaks at 2.5 and 3.08 eV and weaker ones at 2.7, 3.8, and 4.2 eV, whereas the one with $\vec{E} \perp \hat{c}$ has peaks at 2.5, 3.0, 3.37, and 3.88 eV. The corresponding derivative spectra have more fine structures as expected. The reflectivities decrease monotonically for $\hbar\omega \geq 3.5$ eV. At higher temperatures, the structures become less pronounced and shift towards lower energies. They shift by about 0.25 eV from 5 to 300° K. A particularly interesting feature of the spectra is the reflectivity with $\vec{E} \parallel \hat{c}$ is larger than the one with $\vec{E} \perp \hat{c}$ by an overall factor of 1.6 and by a factor as large as 2 for individual peaks.

The reflectivities, $R(\omega)$, for the two different polarizations calculated by the empirical pseudopotential method by C. Y. Fong[69] are shown in Fig. 36. Thermal broadening and the Debye-Waller factors were not considered in the theoretical results. However, the general shapes of these reflectivities for $\hbar\omega \leq 3.0$ eV resemble the measured results at 300° K (Fig. 36). For higher photon energy, the theoretical reflecti-

vities increases. These results differ from the experimental data. All these discrepancies can be attributed to the fact that the bands 29-32 and 41-42 are too close to the gap. Consequently, they contribute too much to the calculated reflectivities above 3.0 eV. They also affect the calculated reflectivities below 3.0 eV through the Kramer-Kronig relation. Fong[69] has calculated $\epsilon_{2\parallel}(\omega)$ and $\epsilon_{2\perp}(\omega)$ by considering only transitions between the top 4 valence bands to the bottom 4 conduction bands. The corresponding reflectivities are also shown in Fig. 36.

Since the lattice constants at low temperature differ from the ones quoted above by 2%[65] and no new structure in the optical data is found at the phase transition, the latter calculated reflectivities can be compared to the ones measured at 5° K. In the case of $\vec{E} \parallel \hat{c}$, peaks in the calculated reflectivity at 2.3, 3.1 and 3.8 eV agree reasonably with the experimental results. The first peak comes mainly from 36 → 37 transitions in the region near Γ and Λ where the dipole matrix elements for $\vec{E} \parallel \hat{c}$ are large. The second peak is due to interband transitions 36 → 37, 38, 39, 40 and 35 → 37, 38 in a large region with k_z, the $\hat{z}$-component of the electron momentum, about halfway between Γ and Z. The region near the XY($\hat{a} - \hat{b}$) plane with transitions of 33, 34 → 36, 37 and 38 contributes also, but the strengths of the dipole matrix elements are weaker. The important contributions to the peak at 3.8 eV come from transitions of 33 → 38 with $0.167 \leq k_z \leq 0.333\left(\frac{2\pi}{c}\right)$. The main peak for $\vec{E} \perp \hat{c}$ is at 2.2 eV and two weak structure are at 3.0 and 3.3 eV. The first peak is caused by transitions of 36 → 37 and 38 near Y and near Σ. The regions involved in these transitions are considerably larger than the 2.3 eV peak in $\vec{E} \parallel \hat{c}$ case, however, the dipole matrix elements for these transitions are smaller and are almost constant throughout the regions. The $\hat{z}$-

components of these matrix elements are mostly zero. Therefore, this peak with $\vec{E} \perp \hat{c}$ is mainly due to increase in the joint density of states. This is in contrast to the corresponding peak with $\vec{E} \parallel \hat{c}$ where the effect of the dipole matrix elements are dominant. The joint density of states at 3.0 eV in $\vec{E} \perp \hat{c}$ are the same as in $\vec{E} \parallel \hat{c}$. Similar to the 2.2 eV structure, the dipole moments are weaker in the case of $\vec{E} \perp \hat{c}$. The slightly higher reflectivity at 3.3 eV compared to the structure at 3.0 eV in both theory and experiment is due to additional contributions of $35 \rightarrow 39$ in the region near XY plane and $35 \rightarrow 40$ transitions near Γ. The overall ratio of the calculated reflectivities for the two polarizations in considering transitions of 4 valence bands to 4 conduction bands is about 1.4. From the above identifications for various structure in the spectra, it is therefore believed that the large optical anisotropy of SbSI is mainly due to the difference in the dipole matrix elements for the two polarizations.

V. CONCLUSION

Wavelength modulation spectroscopy has been very useful in finding the electronic transitions in a large variety of materials. By comparing these results to the optical properties calculated by pseudopotential methods, identification of the structures with critical points in the Brillouin zone can usually be made. In individual materials, observations were frequently made of specific structures of unique character. In PbS, the structures at 5.08 eV are believed to be excitonic. In $ZnGeP_2$, some of the transitions associated with the "pseudodirect" gap are observed. In GaSe, the S1 transition is deduced to be a three-dimensional anisotropic M_0 exciton. Also in GaSe, and in $SnSe_2$ and SnS_2, the localization of some optical transitions around either the cation or anion is demonstrated.

It had been hoped to extend the wavelength modulation spectrometer to the vacuum ultraviolet region of the spectrum. It was for this reason that the system was encased in an aluminum vacuum chamber, a deuterium lamp constructed, and LiF windows were mounted on the sample dewar. The results of this effort were not very satisfactory. The overall signal intensity was not sufficient to do modulation spectroscopy. The reason for this is not clear, but was probably due to the low intensity of the deuterium lamp as compared to the xenon arc lamp used in the near ultraviolet region of the spectrum.

This work was done with support from the U. S. Energy Research and Development Administration.

REFERENCES

1. J. C. Slater, Phys. Rev. 51, 846 (1937).
2. C. Herring, Phys. Rev. 57, 1169 (1940); C. Herring and A. G. Hill, Phys. Rev. 58, 132 (1940).
3. J. C. Phillips and L. Kleinman, Phys. Rev. 116, 287 (1959).
4. H. R. Philipp and E. A. Taft, Phys. Rev. 113, 1002 (1959).
5. B. O. Seraphin, Phys. Rev. 140A, 1716 (1965).
6. W. E. Engeler, H. Fritzsche, M. Garfinkel, and J. J. Tiemann, Phys. Rev. Lett. 14, 1069 (1965); G. W. Gobeli and E. O. Kane, Phys. Rev. Lett. 15, 142 (1965).
7. B. Batz, Solid State Comm. 4, 241 (1965).
8. R. R. L. Zucca and Y. R. Shen, Applied Optics 12, 1293 (1973); R. R. L. Zucca, PhD Thesis, University of California, Berkeley, California, 1971.
9. For a general review of modulation spectroscopy and experimental results see M. Cardona, Solid State Physics, suppl. II, ed. by F. Seitz, D. Turnbull, and H. Ehrenreich, Academic Press, 1969 and Surface Sci. 37 (1972).
10. Bulova American Time Products, Inc., model L-44.
11. J. A. R. Samson, J. Opt. Soc. Am. 54, 6 (1964).
12. W. R. Hunter, Optica Acta 9, 255 (1962).
13. A. S. Coolidge, H. M. James, and R. D. Present, J. Chem. Physics 4, 193 (1936); H. M. James and A. S. Coolidge, Phys. Rev. 55, 184 (1939).
14. N. Sassa, Science of Light 10, 53 (1961).
15. H. W. Bode, Network Analysis and Feedback Amplifier Design (Van

Nostrand, 1945), p. 335.

16. D. M. Roessler, Brit. J. of Appl. Phys. 16, 1119 (1965); 17, 1313 (1966).

17. L. D. Landau and E. M. Lifschitz, Statistical Physics 2nd edition, (Addison-Wesley, 1969), p. 370.

18. S. E. Kohn, P. Y. Yu, Y. Petroff, Y. R. Shen, Y. Tsang, and M. L. Cohen, Phys. Rev. b8, 1477 (1973).

19. M. Cardona and D. L. Greenaway, Phys. Rev. A133, 1685 (1964).

20. D. L. Mitchell, E. D. Palik, and J. N. Zemel, Physics of Semiconductors, Paris, 1964, ed. M. Hulin (Academic Press, New York, 1964), p. 325.

21. D. E. Aspnes and M. Cardona, Phys. Rev. 173, 714 (1968).

22. Y. Petroff, S. Kohn, and Y. R. Shen, Surface Sci. 37, 591 (1973).

23. Y. Toyozawa, M. Inoue, M. Okazaki, and E. Hanamura, J. Jap. Phys. Soc. Suppl. 21, 133 (1967).

24. Y. W. Tung and M. L. Cohen, Phys. Rev. 180, 283 (1969); Phys. Rev. B2, 1216 (1970); Phys. Lett. A29, 236 (1969).

25. C. Varea de Alvarez, J. P. Walters, M. L. Cohen, J. Stokes, and Y. R. Shen, Phys. Rev. B6, 1412 (1972).

26. S. E. Stokowski, Phys. Rev. B6, 1294 (1972).

27. C. Varea de Alvarez, M. L. Cohen, S. E. Kohn, Y. Petroff, and Y. R. Shen, Phys. Rev. B10, 5175 (1974).

28. R. A. Bendorius, G. Z. Krivaite, A. Yu. Shileika, G. F. Karavaev, and Y. A. Chaldyshev, International Conference on Semiconductors, Warsaw (1972), unpublished; A. Raudonis, V. S. Grigoreva, V. D. Prochukhan, and A. Shileika, Phys. Stat. Solidi B57, 415 (1973); A. Shileika, Surface Sci. 37, 730 (1973).

29. J. L. Shay, B. Tell, E. Buehler, and J. H. Wernick, Phys. Rev. Lett. 30, 983 (1973).

30. J. J. Hopfield, J. Phys. Chem. Solids, 15, 97 (1960).

31. J. L. Shay, E. Buehler, and J. H. Wernick, Phys. Rev. B2, 4104 (1970); 3, 2004 (1971); J. L. Shay and E. Buehler, ibid, 3, 2598 (1971); 4, 2479 (1971); C. C. Y. Kwan and J. C. Woolley, Can. J. Phys. 48, 2085 (1970); Phys. Status Solidi B44, K93 (1971); Appl. Phys. Lett. 18, 520 (1971); R. E. Karymahakov. Y. I. Ukhanov, and Y. V. Shmartsev, Fiz. Tekh. Poluprov. 5, 514 (1971) [Sov. Phys.-Semicond. 5, 450 (1971)].

32. K. Schubert, E. Dorre, and M. Kluge, Z. Metallk. 46, 216 (1955); F. Jellinek and H. Hahn, Z. Naturf. 16B, 713 (1961).

33. Z. S. Basinski, D. B. Dove, and E. Mooser, Helv. Phys. Acta 34, 373 (1961); J. C. J. M. Terhel and R. M. A. Lieth, Phys. Status Solidi (a) 10, 529 (1972).

34. G. Ottaviani, C. Canali, F. Nava, Ph. Schmid, E. Mooser, R. Minder, and I. Zschokke, Sol. State Comm. 14, 933 (1974).

35. M. Schlüter, J. Camassel, S. E. Kohn, J. P. Voitchovsky, Y. R. Shen, and M. L. Cohen, Phys. Rev. B13, 3534 (1976).

36. E. Mooser and M. Schlüter, Il Nuovo Cimento 18B, 164 (1973).

37. V. K. Subashiev, Le-Khac-Binh, and L. S. Chertkova, Solid State Comm. 9, 369 (1971).

38. V. I. Sokolov, D. B. Kushev, and V. K. Subashiev, Physica Status Solidi B50, K125 (1972).

39. Y. Suzuki and Y. Hamakawa, J. Phys. Soc. Japan 37, 108 (1974).

40. A. Balzaroth, M. Piacentini, E. Burattini, and P. Picozzi, J. Phys. C4, L273 (1971).

41. Y. Sasaki, C. Hamaguchi, and J. Nakai, J. Phys. C5, L95, (1972).

42. A. Balzarotti and M. Piacentini, Solid State Comm. 10, 421 (1972).

43. Y. Sasaki, C. Hamaguchi, and J. Nakai, J. Phys. Soc. Japan 38, 162 (1975).

44. R. J. Elliot, Phys. Rev. 108, 1384 (1957).

45. M. Shinada and S. Sugano, J. Phys. Soc. Japan 21, 1936 (1966).

46. E. O. Kane, Phys. Rev. 180, 852 (1963).

47. A. Baldereschi and M. G. Diaz, Nuovo Cimento 68B, 217 (1970); J. A. Deverin, Helva Phys. Acta 42, 397 (1969).

48. E. Aulich, J. L. Brebner, and E. Mooser, Phys. Status Solidi 31, 129 (1969).

49. N. P. Gavaleshko, M. V. Kurik, A. S. Savtchuk, and G. B. Delevskii, Phys. Status Solidi B65, K19 (1974).

50. D. L. Greenaway and R. Nitsche, J. Phys. Chem. Solids 26, 1445 (1965).

51. G. Domingo, R. S. Itoga, and C. R. Kannewurf, Phys. Rev. 143, 536 (1966).

52. P. A. Lee and G. Said, Brit. J. Appl. Phys., J. Phys. D1, 837 (1968).

53. P. A. Lee, G. Said, R. Davis, and T. H. Lim, J. Phys. Chem. Solids 30, 2719 (1969).

54. B. L. Evans and R. A. Hazelwood, Brit. J. of Appl. Physics, J. of Physics, D2, 1507 (1969).

55. V. V. Sobolev and V. I. Donetskich, Phys. Status Solidi 42, K53 (1970).

56. J. Camassel, M. Schluter, S. Kohn, J. P. Voitchovsky, Y. R. Shen, and M. L. Cohen, Phys. Status Solidi 75, 303 (1976).

57. C. Y. Fong and M. L. Cohen, Phys. Rev. B5, 3095 (1972).

58. I. Ch. Schluter and M. Schluter, Phys. Status Solidi B57, 145 (1973).

59. D. L. Greenaway and R. Nitsche, J. Phys. Chem. Sol. 26, 1445 (1965).

60. L. E. Conroy and K. C. Park, Jung. Chem. 7, 459 (1968).

61. A. R. Beal, J. C. Knights, and W. Y. Liang, J. Phys. C5, 3531 (1972).

62. R. B. Murray, R. A. Bromley, and A. D. Yoffe, J. Phys. C5, 746 (1972).

63. L. F. Mattheiss, Phys. Rev. B8, 3719 (1973).

64. C. Y. Fong, J. Camassel, S. E. Kohn, and Y. R. Shen, Phys. Rev. B13, 5442 (1976).

65. For example, A. Kirkuchi, Y. Oka, and E. Sawaguchi, J. Phys. Soc. Japan 23, 337 (1967).

66. For example, D. M. Bercha, V. Yu Slivka, N. N. Syrbu, I. D. Turganitsa, and D. V. Chepur, Fiz. Tverd. Tela. 13, 276 (1971) (Trans. Sov. Phys.-Solid State, 13, 217 (1971)).

67. D. Berlincourt, H. Jaffe, W. Merz, and R. Nitsche, Appl. Phys. Lett. 4, 61 (1964).

68. H. G. Haffle, H. Wachernig, C. Irslinger, R. Grisar, and R. Nitsche, Phys. Status Solidi 42, 531 (1970).

69. C. Y. Fong, Y. Petroff, S. Kohn, and Y. R. Shen, Solid State Comm. 14, 681 (1974).

FIGURE CAPTIONS

1. Schematic of the focusing optics on the entrance to the monochrometer. Mirror M2 is a vibrating mirror which oscillates as indicated by the arrow. Slit S2 of the monochrometer is wide open.
2. Schematic of the optical system for the sample and detector. Mirror M6 is a chopper mirror rotating at 5 Hz. The sample sits in a helium cryrostat which is not shown. The four compensating windows in the reference beam are to compensate for the two passes through the two cryrostat windows.
3. Block diagram of the electronic instrumentation for wavelength modulation spectroscopy.
4. Block diagram of the 6 KHz feedback loop and a schematic for the preamplifier.
5. Cross-section view of the deuterium lamp. Only one feedthrough for the filament is shown.
6. Spectrum of deuterium lamp. The intensity is in arbitrary units. No correction has been made for dispersion of the photomultiplier sensitivity or the monochrometer efficiency.
7. Reflectivity and derivative reflectivity of PbTe at 5° K. The dotted curve is the theoretical $(1/R)dR/d\omega$ spectra calculated by EPM.
8. Reflectivity and derivative reflectivity of PbSe at 5° K. The dotted curve is the theoretical $(1/R)dR/d\omega$ spectra calculated by EPM.
9. Reflectivity and derivative reflectivity of PbS at 5° K. The dotted curve is the theoretical $(1/R)dR/d\omega$ spectra calculated by EPM.
10. $\varepsilon_1(\omega)$ and $\varepsilon_2(\omega)$ of (a) PbTe, (b) PbSe, and (c) PbS calculated by Kramers-Krönig analysis of the $(1/R)dR/d\omega$ spectra.

11. $d\varepsilon_1/d\omega$ and $d\varepsilon_2/d\omega$ of (a) PbTe, (b) TbSe, and (c) PbS calculated by Kramers-Krönig analysis of the $(1/R)dR/d\omega$ spectra.
12. Temperature dependence of the derivative reflectivity $(1/R)dR/d\omega$ of PbS around the E_3 structure.
13. Crystal structure of $ZnGeP_2$.
14. Derivative spectra $(1/R)dR/d\omega$ of $ZnGeP_2$ at 5° K for parallel (——) and perpendicular (---) polarization. For comparison, the derivative spectrum of GaP (-·-) is also given.
15. Reflectivity of $ZnGeP_2$ at 5° K and at 300° K.
16. Comparison of the theoretical and epxerimental reflectivity for $ZnGeP_2$ in the parallel and perpendicular polarizations.
17. Experimental (full line) and calculated[35] (broken line) reflectivity of GaSe. The theoretical curve has been shifted by 0.4 eV to higher energies. Structures in the experimental spectrum are labelled according to Table III. The corresponding labelling of the theoretical curve refers to $\underset{\sim}{k}$-space location and polarization dependence of the transitions involved.
18. First energy derivative spectrum obtained from the measured (full line) and theoretical[35] (broken line) reflectivity of Fig. 17. The shift of the theoretical curve and the labelling is as in Fig. 17.
19. Several room and low temperature spectra of the S1 structure in GaSe around 3.4 eV. (a) Room temperature wavelength modulated reflectivity spectrum, (b) differential electroreflectance spectrum at room temperature, (c) room temperature reflectivity spectrum, (d) reflectivity spectrum at 5° K. Note the well resolved doublet structure.

20. Reflectivity spectra of ten GaS_xSe_{1-x} mixed crystals measured at 5° K between 3 eV and 6 eV.

21. Energy diagram of structures observed in the GaS_xSe_{1-x} mixed crystal reflectivity which exhibit $\Delta \approx 0$ energy shift. The structures are labelled G1 to G4 indicating the predominant anion (gallium) character in the wavefunctions of initial and final states. Well resolved structures are indicated by circles, weak structures by triangles.

22. Energy diagram of reflectivity structures of GaS_xSe_{1-x} labelled GS1 to GS6, exhibiting intermediate ($\Delta \approx 400$ meV) energy shift. The labelling refers to mixed cation (Ga) and anion (Se, S) character of the involved functions.

23. Experimental (full line) and calculated model (broken line) reflectivity of structures around 4.0 eV in GaS. A two-dimensional M_0 c.p. exciton model and its associated continuum transition are used in the model reflectivity as explained in the text.

24. Energy diagram of reflectivity structures of GaS_xSe_{1-x}, labelled S1 to S4, exhibiting strong ($\Delta \approx 780$ meV energy shift. The labelling refers to predominant anion (Se, S) character of the involved wavefunctions.

25. Experimental reflectivity spectra (5° K) of the double structure in S1 in a) GaSe around 3.4 eV and b) GaS around 4.6 eV.

26. Reflectivity spectrum of SnS_2 at 5° K and room temperature between 2 eV and 6 eV.

27. Wavelength modulated reflectivity spectrum of SnS_2 at 5° K and room temperature.

28. Reflectivity spectrum of $SnSe_2$ and room temperature between 2 eV

and 6 eV.

29. Wavelength modulated reflectivity spectrum of $SnSe_2$ at 5° K and room temperature.

30. Comparison of the experimental (5° K) and calculated (Ref. 10) reflectivity spectra of SnS_2.

31. Temperature dependence of the experimental differential reflectivity spectra of SnS_2.

32. Comparison of the experimental (5° K) and calculated (Ref. 58) reflectivity spectra of $SnSe_2$.

33. The wavelength modulated reflectivity at 5° K and the reflectivity at 5° K (——) and at 300° K (---).

34. The experimental and theoretical spectra of HfS_2. The theoretical spectra was calculated by EPM by Fong.[64]

35. Measured reflectivities and wavelength modulated reflectivities of SbSI at 5° K and 300° K. Arrows on the curves indicate the axis of the scale.

36. Comparison between the experimental reflectivity and the calculated reflectivity of Fong.[69] The calculated reflectivity is for the room temperature paraelectric crystal structure. The experimental spectra is at 5° K in the ferroelectric phase.

TABLE CAPTIONS

I. Critical point energies of (a) PbTe, (b) PbSe, and (c) PbS. The second column contains critical points derived from experimentally measured $(1/R)dR/d\omega$. [(w) stands for weak.] The third column has critical points from $d\varepsilon_2/d\omega$ spectra obtained by Kramers-Krönig analysis. The fourth column contains the results of EPM calculations.[18]

II. Theoretical[27] and experimental reflectivity structure and their identification for $ZnGeP_2$.

III. Listing of experimental (5° K) energies for the main structures in the reflectivity spectrum of GaSe. The theoretical assignment of k-space location, polarization and band numbers of the involved transitions are also listed.[35] The experimental (5° K) energies of corresponding structures in GaS are given in the last column.

IV. Reduced effective masses of bands 16 and 19 at the Γ-point in GaSe as obtained from various electro-absorption and electro-reflectance measurements and from several theoretical models involved to explain the structure S1 around 3.4 eV in GaSe.

V. SnS_2: Comparison of the low energy structure obtained in differential reflectivity with the indirect forbidden edge reported in absorption.

VI. Listing of experimental energies for the main structures in the reflectivity spectrum of SnS_2 (300° K, 5° K) and results of previous experiments. The theoretical assignment,[57] k-space location, and band numbers of the prominent transitions are also listed.

VII. Listing of experimental energies for the main structures in the reflectivity spectrum of $SnSe_2$. We give also the results of previous

experiments for comparison. The theoretical assignment,[58] k-space location, and band number of the prominent transitions are also listed.

VIII. Comparison of experimental and theoretical[64] critical point energies and their assignment. All energies in eV.

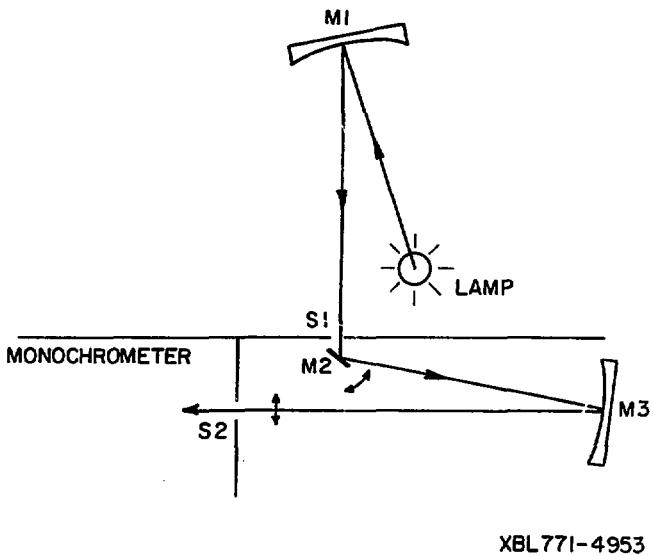

FIGURE 1

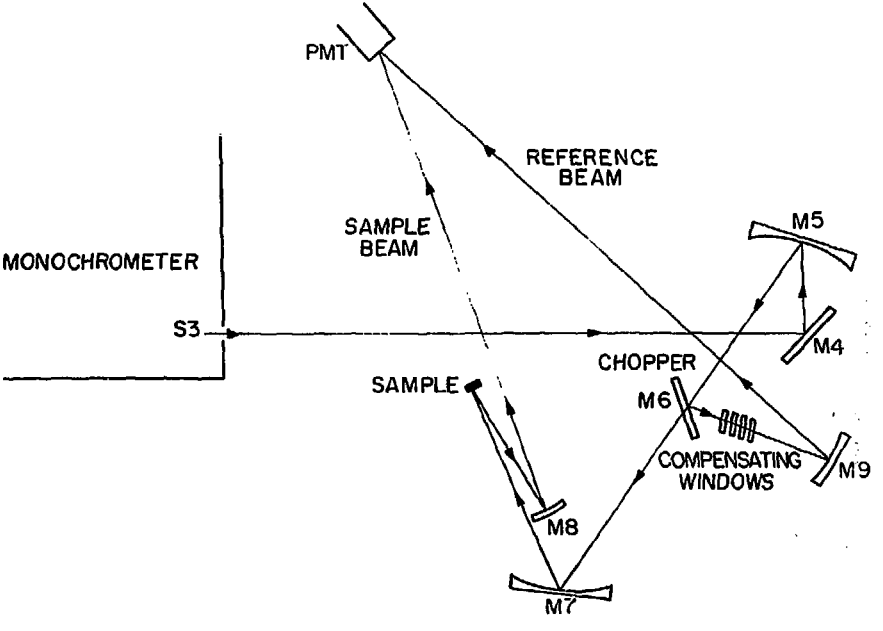
PMT
REFERENCE BEAM
SAMPLE BEAM
MONOCHROMETER
S3
M5
M4
CHOPPER
SAMPLE
M6
COMPENSATING WINDOWS
M9
M8
M7
XBL 771-4954

Figure 2

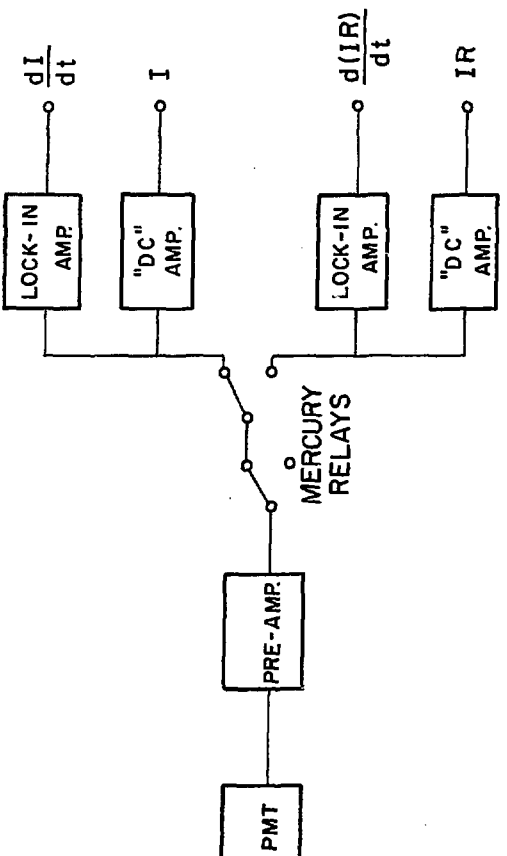
dI/dt
I
d(IR)/dt
IR
LOCK-IN AMP.
"DC" AMP.
LOCK-IN AMP.
"DC" AMP.
MERCURY RELAYS
PRE-AMP.
PMT
XBL 771-4955

Figure 3

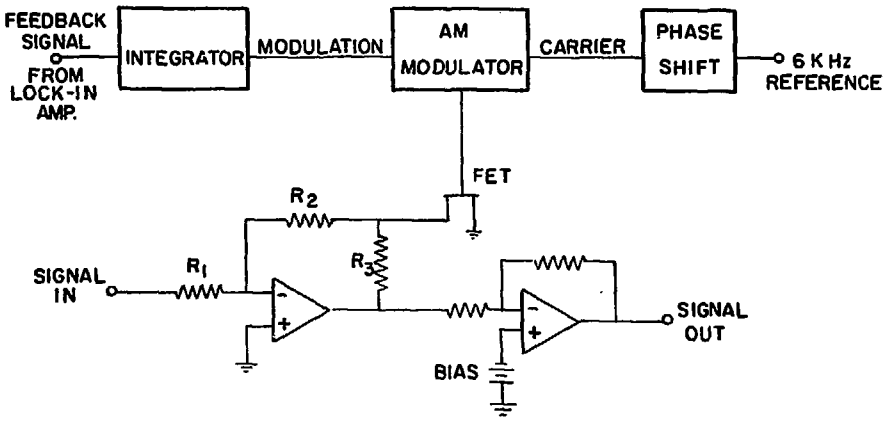
FEEDBACK SIGNAL
FROM LOCK-IN AMP.
INTEGRATOR
MODULATION
AM MODULATOR
CARRIER
PHASE SHIFT
6 K Hz REFERENCE
FET
R2
R3
R1
SIGNAL IN
SIGNAL OUT
BIAS
XBL771-4956

Figure 4

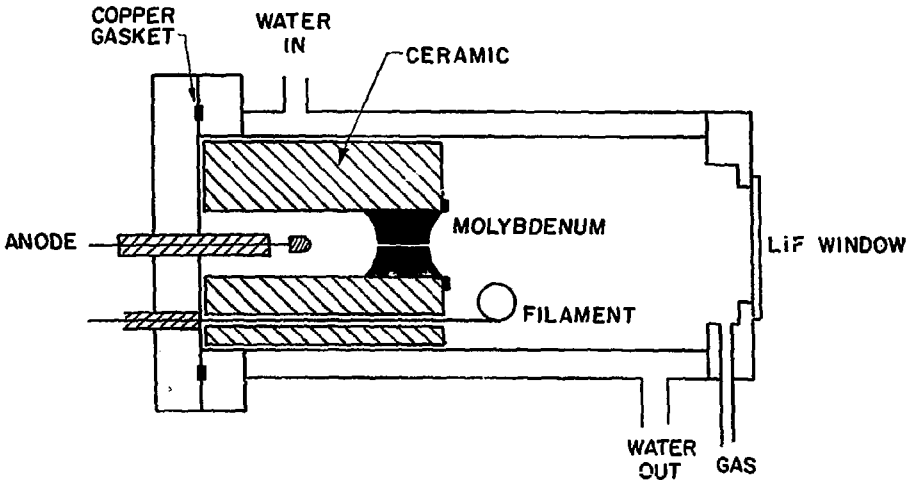
COPPER
GASKET
WATER
IN
CERAMIC
ANODE
MOLYBDENUM
LiF WINDOW
FILAMENT
WATER
OUT
GAS
XBL 771-4957

Figure 5

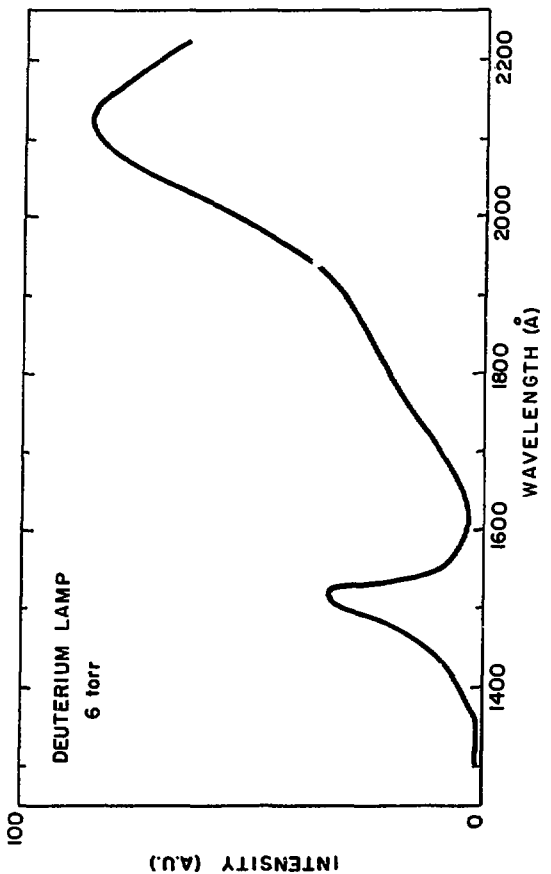

XBL 771-4958

Figure 6

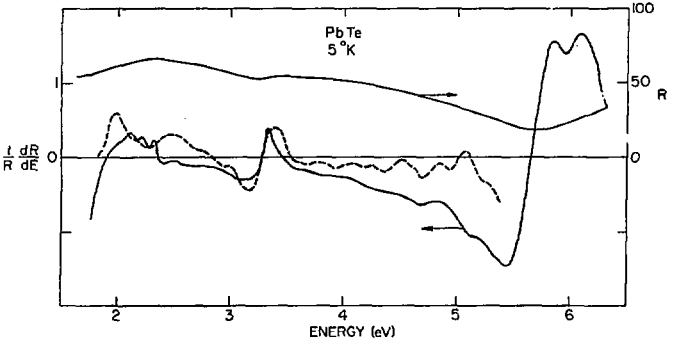
PbTe
5°K
100
50
R
1
0
$\frac{1}{R}\frac{dR}{dE}$
0
2
3
4
5
6
ENERGY (eV)
XBL 723-6082

FIGURE 7

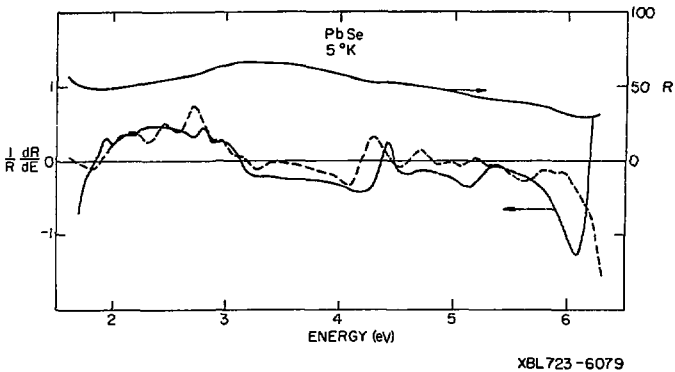
PbSe
5 °K
100
50 R
0
1
0
-1
$\frac{1}{R}\frac{dR}{dE}$
2
3
4
5
6
ENERGY (ev)
XBL723-6079

FIGURE 8

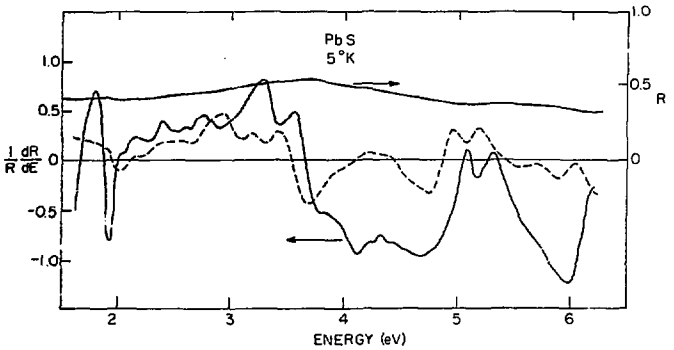

XBL 726-6469

FIGURE 9

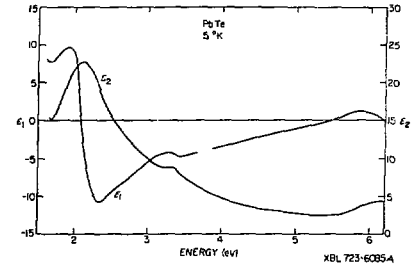

A

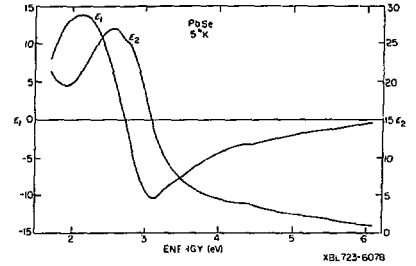

B

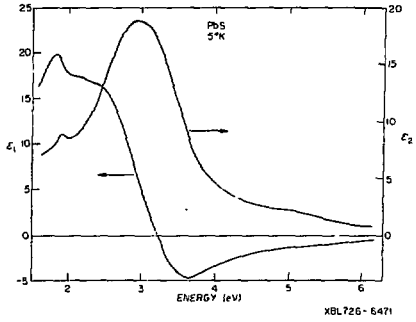

C

FIGURE 10

A

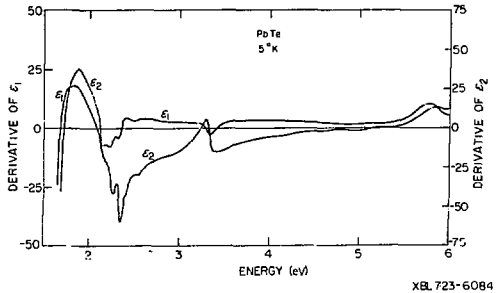

B

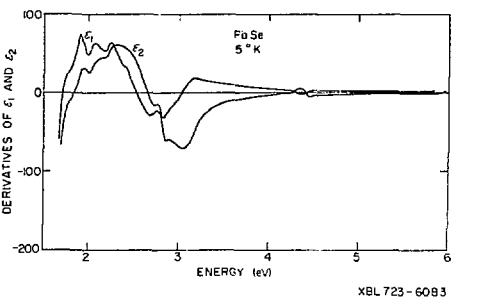

C

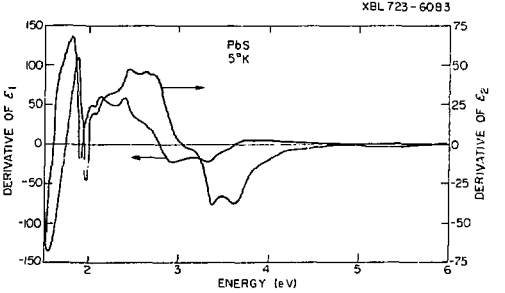

FIGURE 11

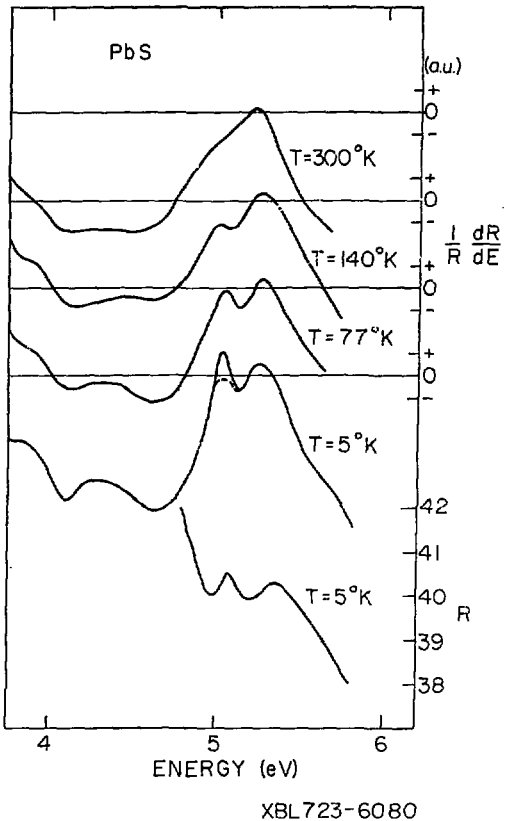
PbS
(a.u.)
T=300°K
T=140°K
T=77°K
T=5°K
T=5°K
1/R dR/dE
R
42
41
40
39
38
4
5
6
ENERGY (eV)
XBL723-6080

FIGURE 12

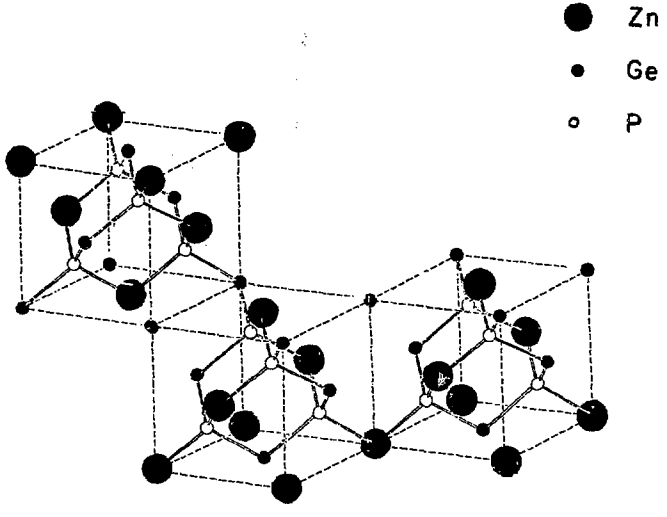

XBL 743-5797

FIGURE 13

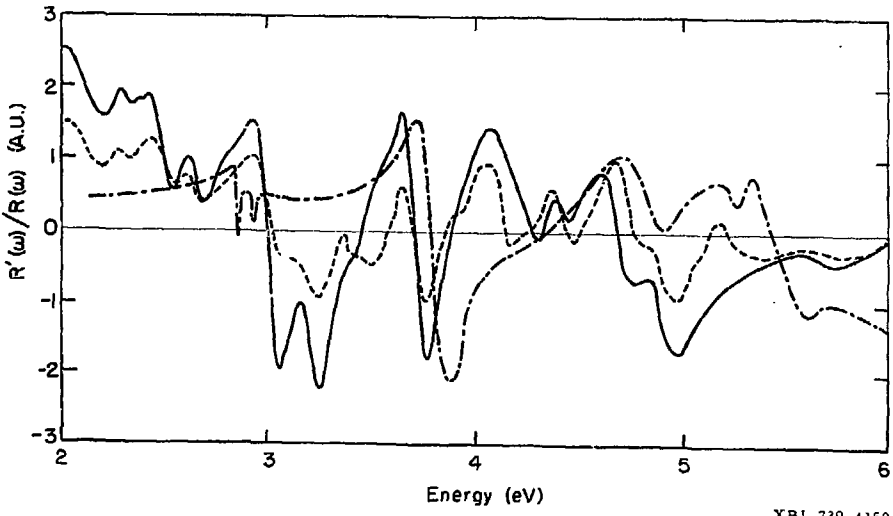

Figure 14

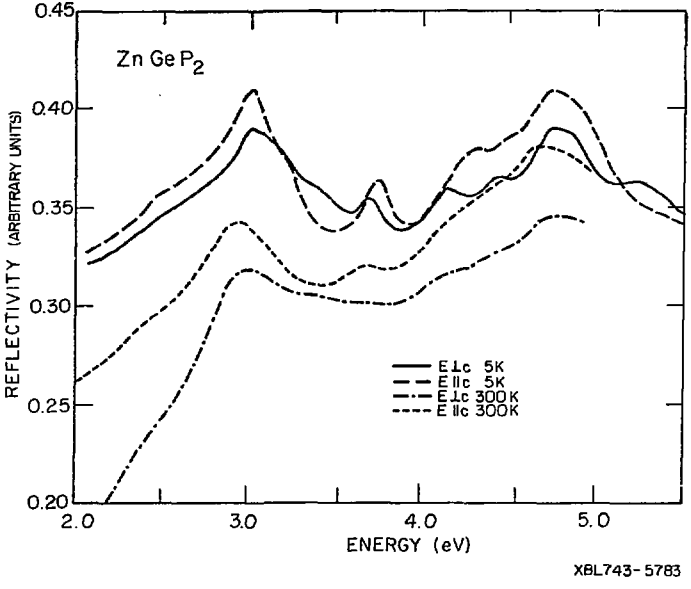
Zn Ge P2
REFLECTIVITY (ARBITRARY UNITS)
0.45
0.40
0.35
0.30
0.25
0.20
2.0
3.0
4.0
5.0
ENERGY (eV)
E⊥c 5K
E∥c 5K
E⊥c 300K
E∥c 300K
XBL743-5783

FIGURE 15

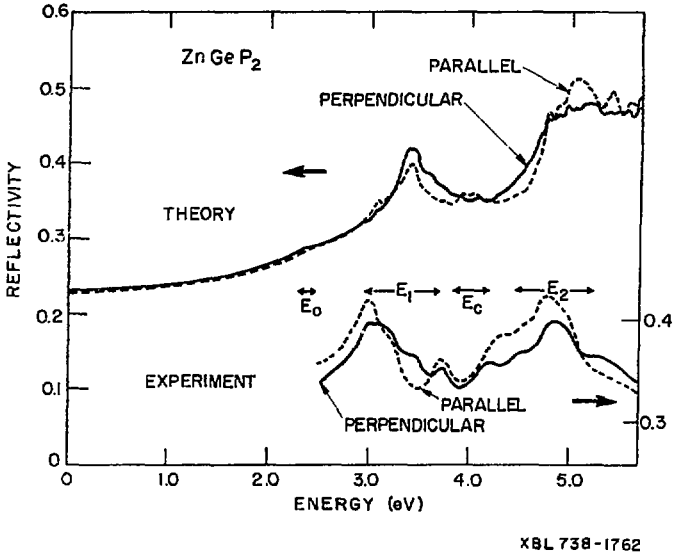

XBL 738-1762

FIGURE 16

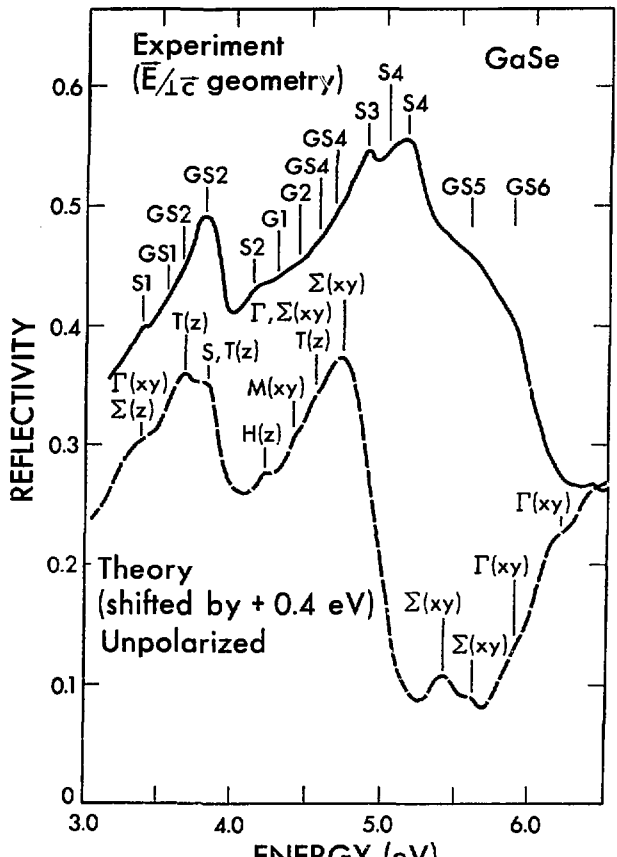

XBL 7710-6802

FIGURE 17

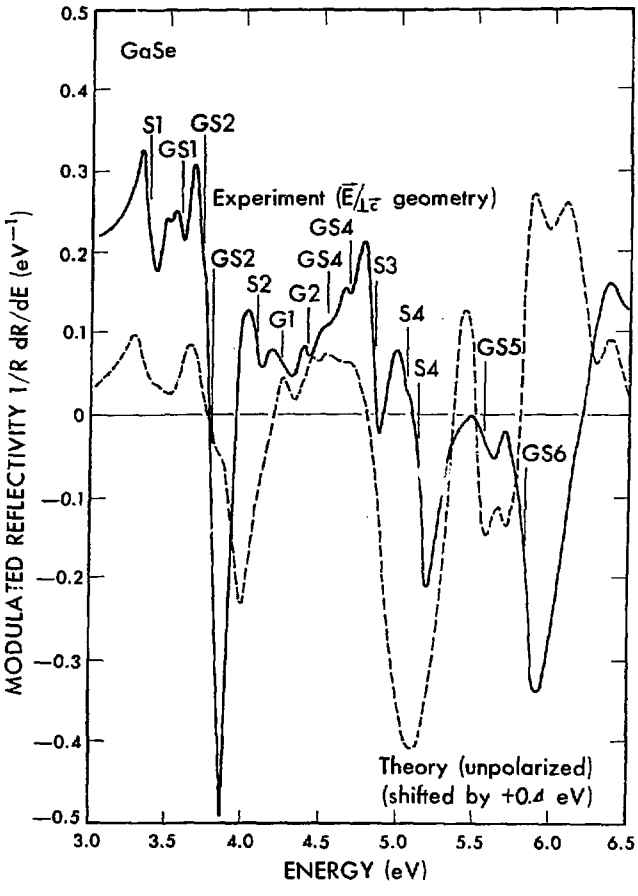

XBL 7710-6801

FIGURE 18

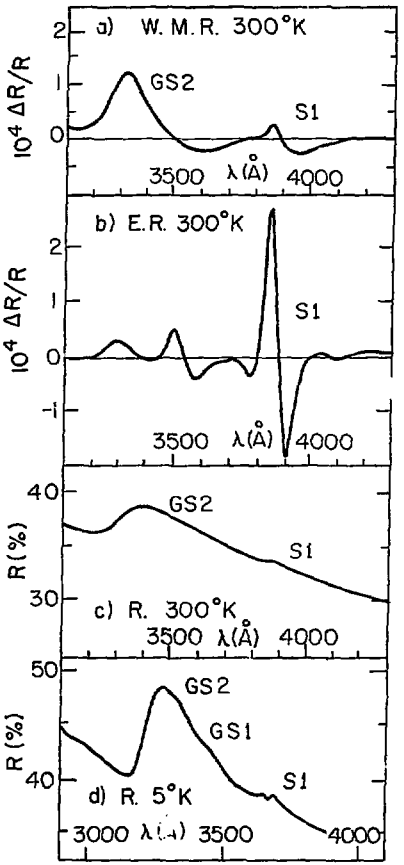
a) W. M. R. 300°K
GS2
S1
$10^4 \Delta R/R$
2
1
0
3500 λ(Å) 4000
b) E. R. 300°K
S1
$10^4 \Delta R/R$
2
1
0
-1
3500 λ(Å) 4000
GS2
S1
R(%)
40
30
c) R. 300°K
3500 λ(Å) 4000
GS2
GS1
S1
R(%)
50
40
d) R. 5°K
3000 λ(Å) 3500 4000
XBL757-6766

FIGURE 19

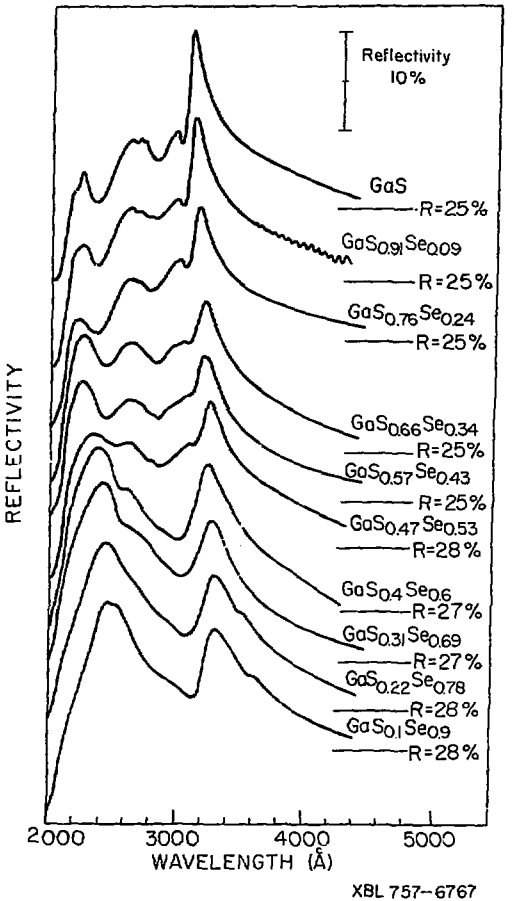
Reflectivity
10%
GaS
R=25%
GaS0.91Se0.09
R=25%
GaS0.76Se0.24
R=25%
GaS0.66Se0.34
R=25%
GaS0.57Se0.43
R=25%
GaS0.47Se0.53
R=28%
GaS0.4Se0.6
R=27%
GaS0.31Se0.69
R=27%
GaS0.22Se0.78
R=28%
GaS0.1Se0.9
R=28%
REFLECTIVITY
2000
3000
4000
5000
WAVELENGTH (Å)
XBL 757-6767

FIGURE 20

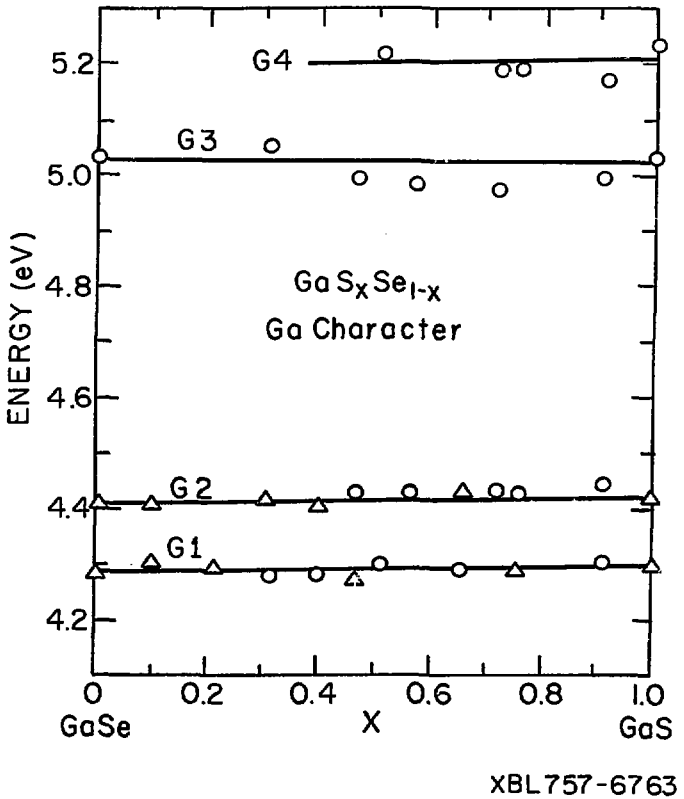
5.2
5.0
4.8
4.6
4.4
4.2
ENERGY (eV)
G4
G3
G2
G1
GaSxSe1-x
Ga Character
0
0.2
0.4
0.6
0.8
1.0
GaSe
X
GaS
XBL757-6763

FIGURE 21

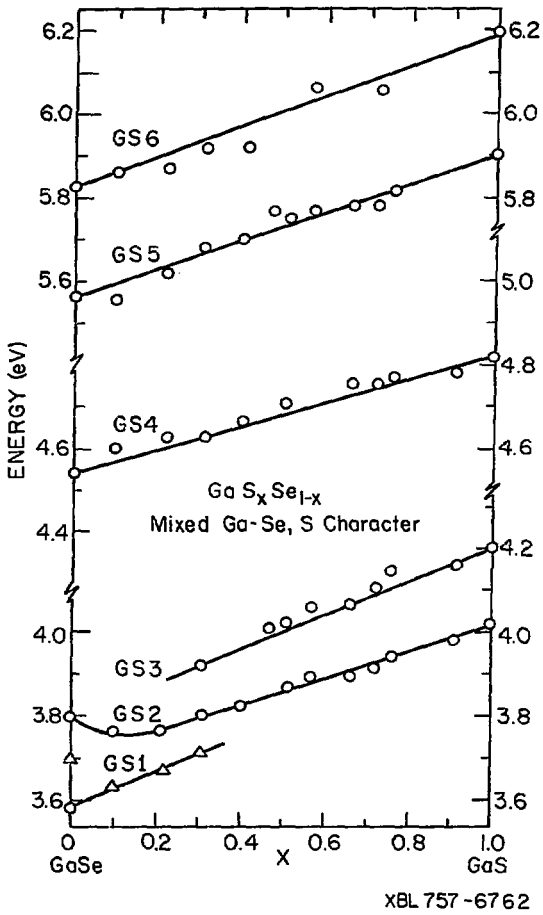
6.2
6.0
5.8
5.6
5.0
4.8
4.6
4.4
4.2
4.0
3.8
3.6
ENERGY (eV)
GS6
GS5
GS4
GS3
GS2
GS1
Ga S$_x$ Se$_{1-x}$
Mixed Ga-Se, S Character
0
0.2
0.4
0.6
0.8
1.0
X
GaSe
GaS
XBL 757-6762

FIGURE 22

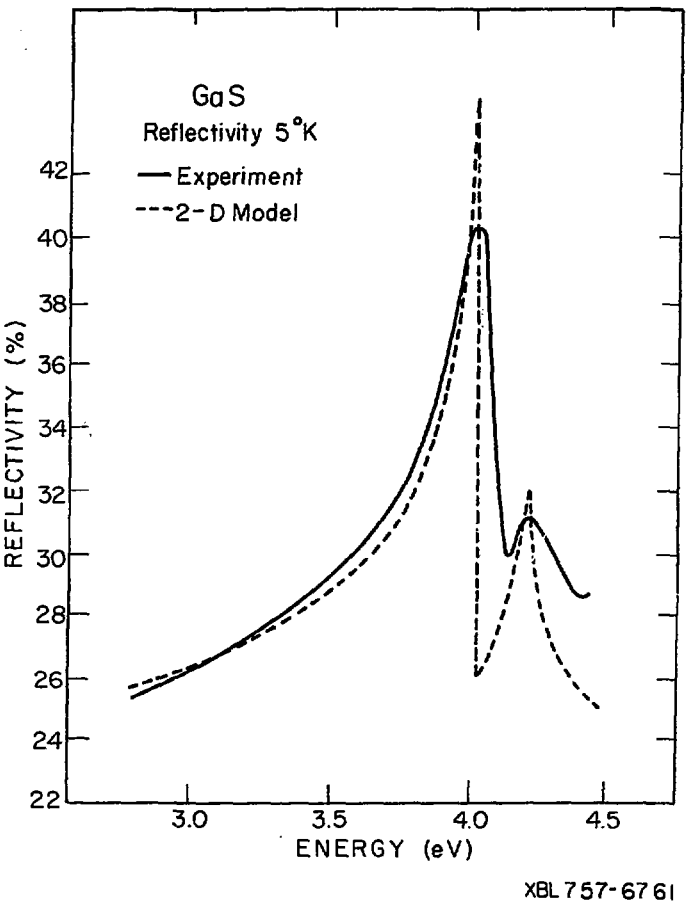
GaS
Reflectivity 5°K
Experiment
2-D Model
REFLECTIVITY (%)
42
40
38
36
34
32
30
28
26
24
22
3.0
3.5
4.0
4.5
ENERGY (eV)
XBL757-6761

FIGURE 23

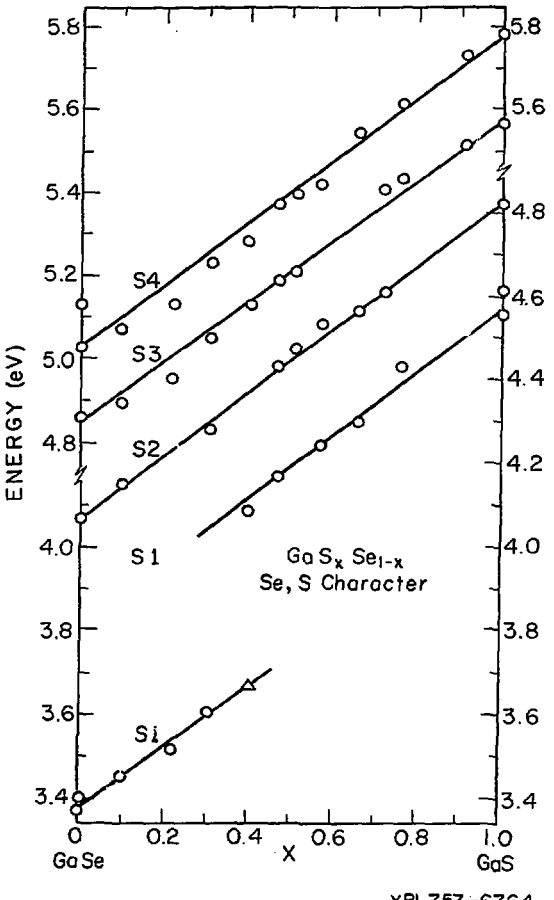
ENERGY (eV)
5.8
5.6
5.4
5.2
5.0
4.8
4.6
4.4
4.2
4.0
3.8
3.6
3.4
S4
S3
S2
S1
Si
GaSx Se1-x
Se, S Character
0
0.2
0.4
0.6
0.8
1.0
X
GaSe
GaS
XBL757-6764

FIGURE 24

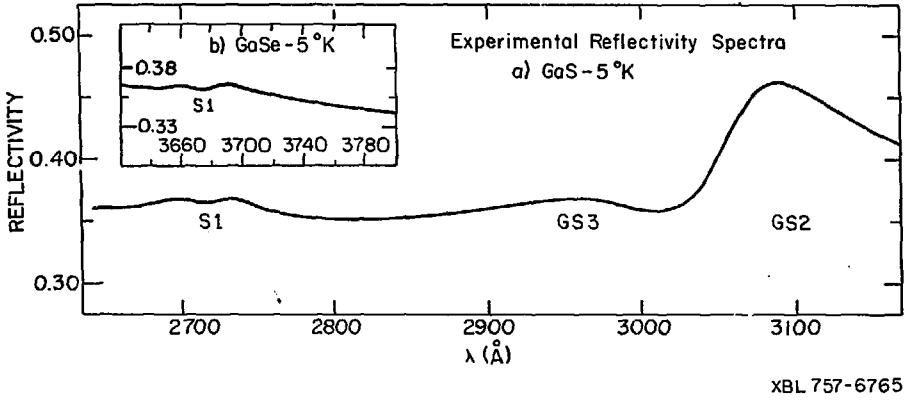
b) GaSe - 5 °K
0.38
S1
0.33
3660 3700 3740 3780
Experimental Reflectivity Spectra
a) GaS - 5 °K
REFLECTIVITY
0.50
0.40
0.30
S1
GS3
GS2
2700
2800
2900
3000
3100
λ (Å)
XBL 757-6765

Figure 25

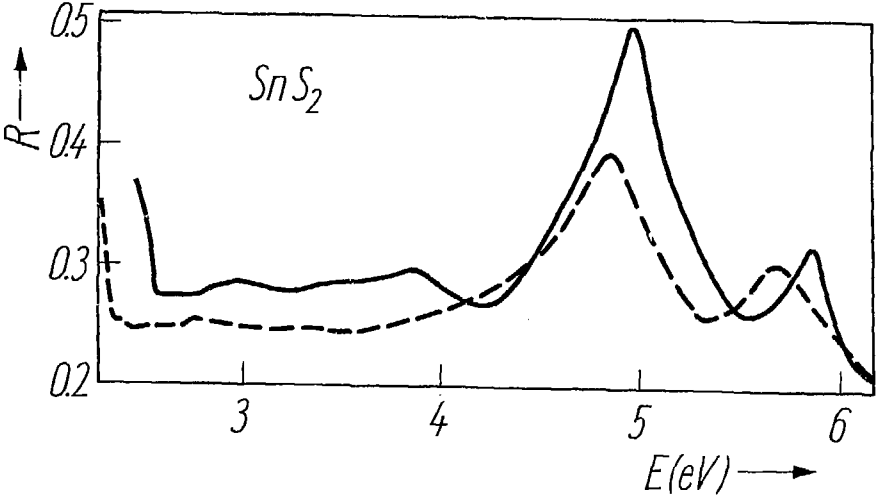

XBL 779-4898

Figure 26

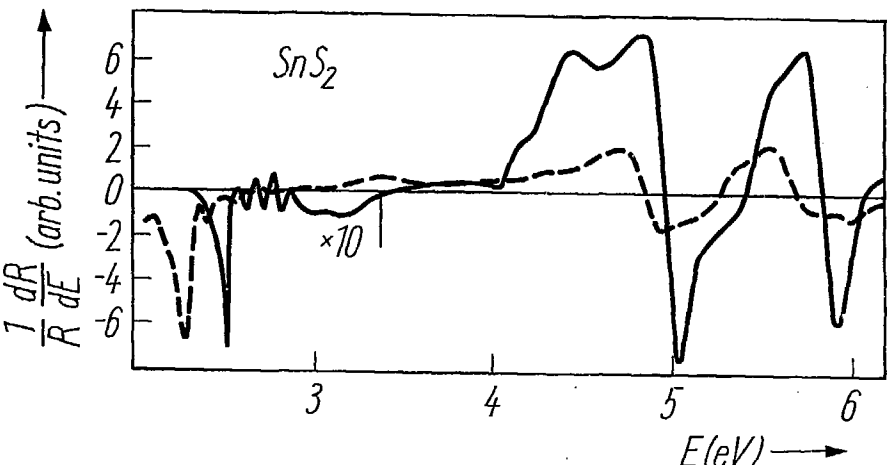

Figure 27

XBL 779-4892

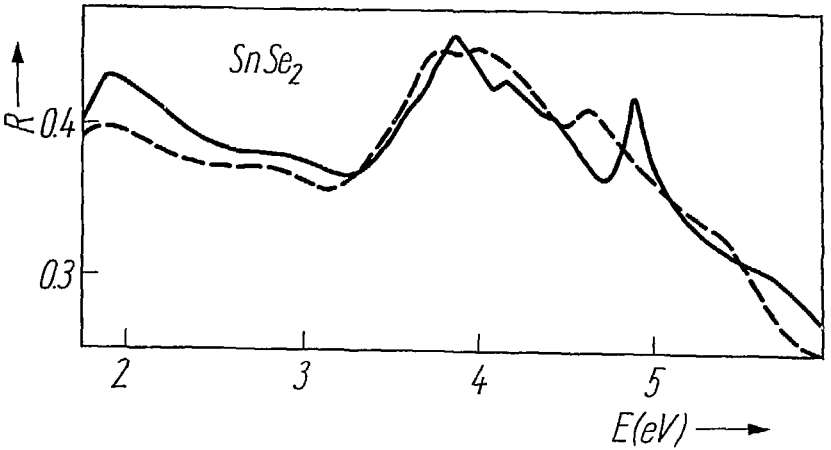

XBL 779-4893

Figure 28

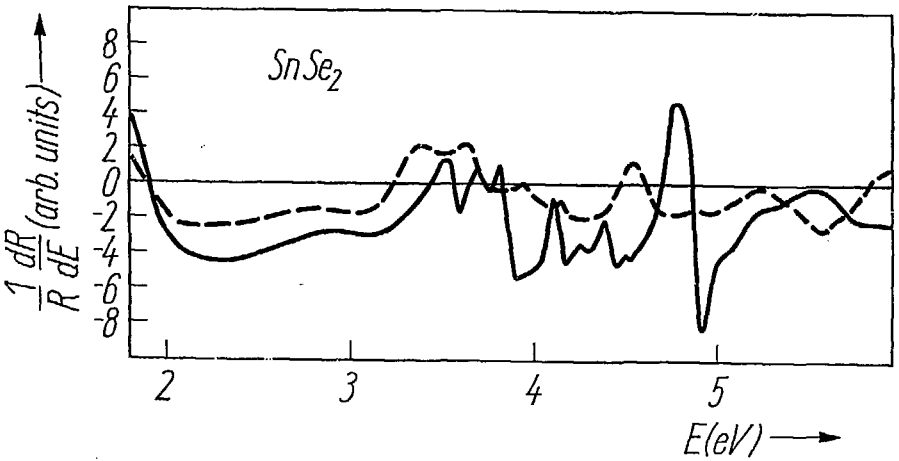

XBL 779-4894

Figure 29

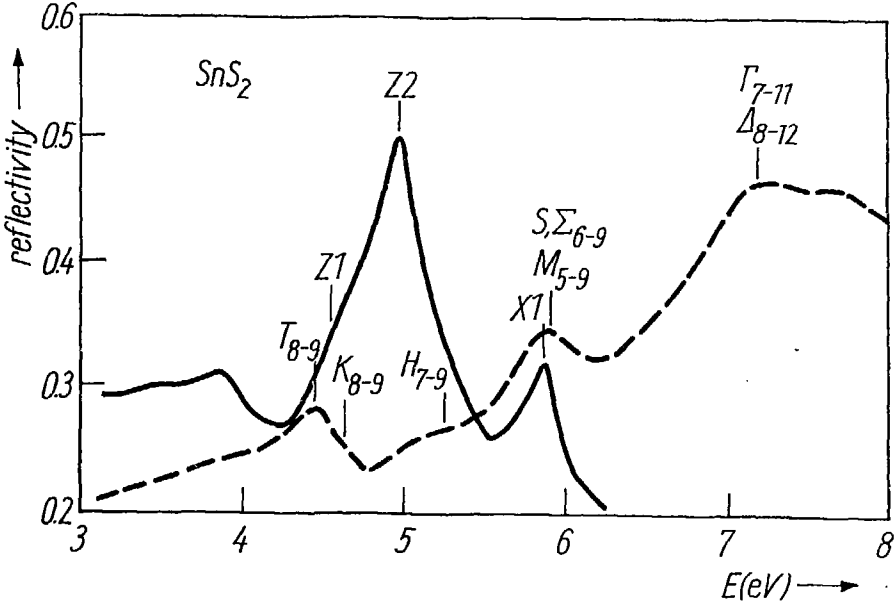

Figure 30

XBL 779-4897

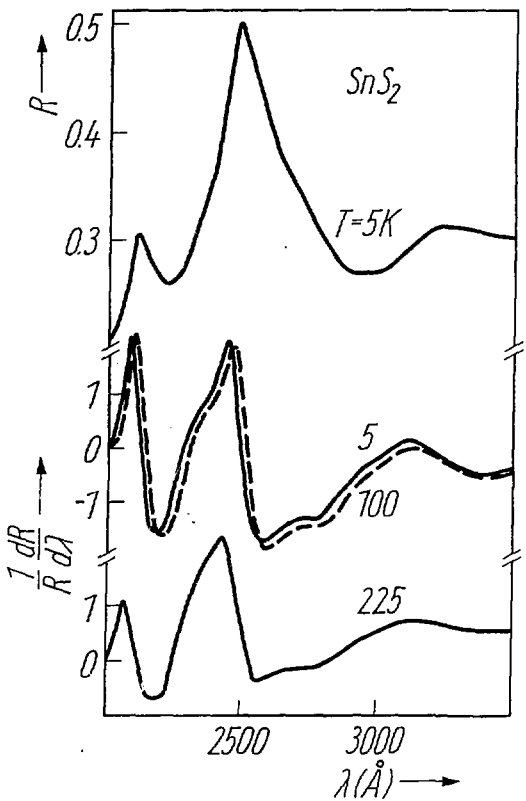

XBL 779-4895

FIGURE 31

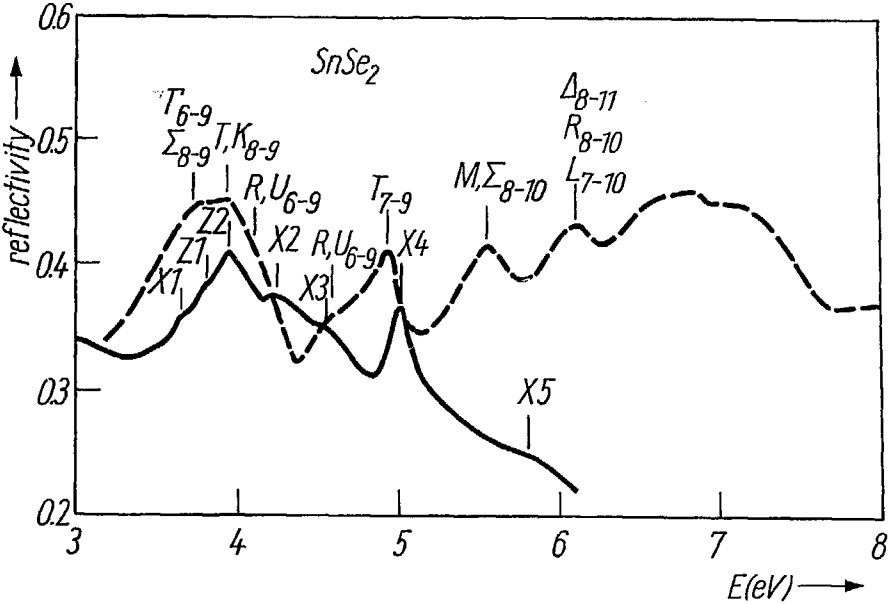

XBL 779-4896

Figure 32

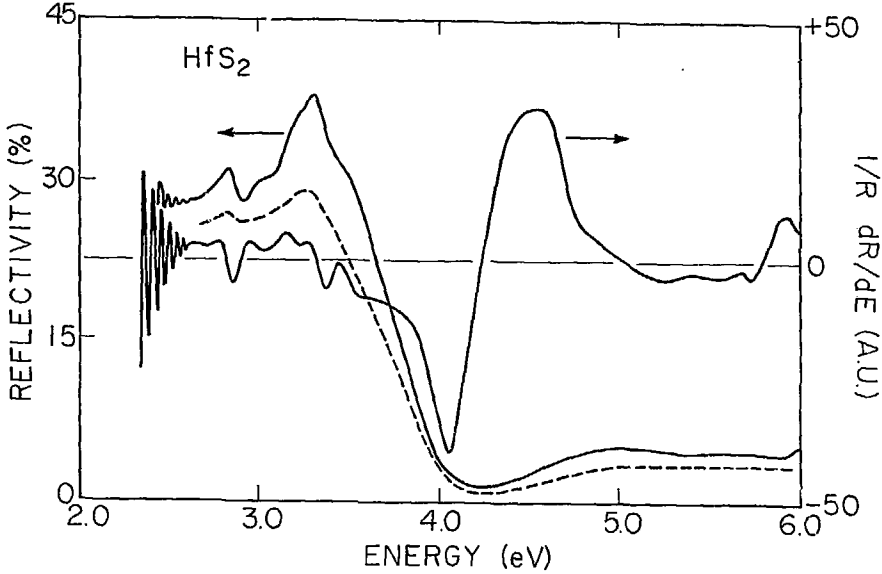

XBL 7511-7581

Figure 33

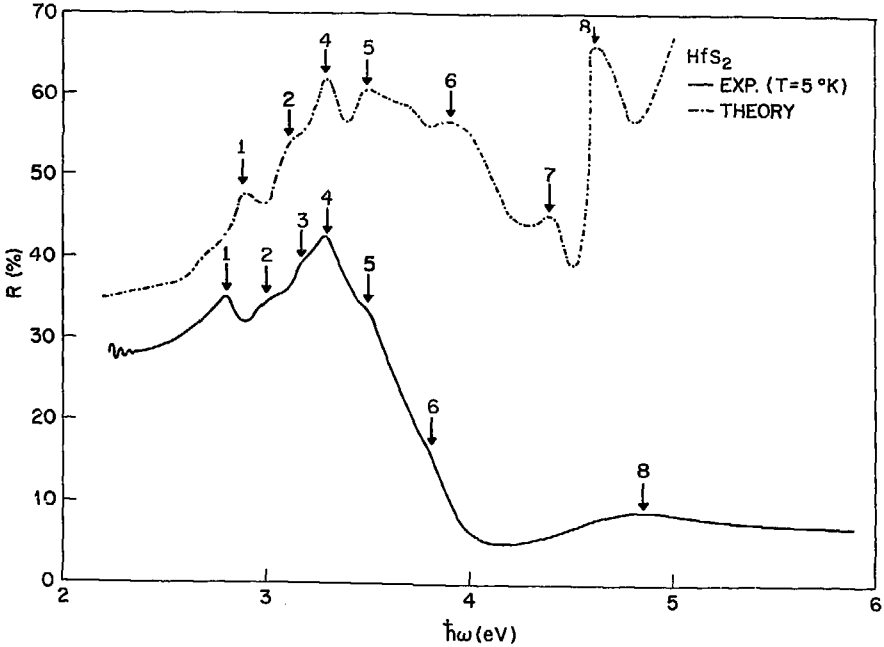

XBL 761-6179

Figure 34

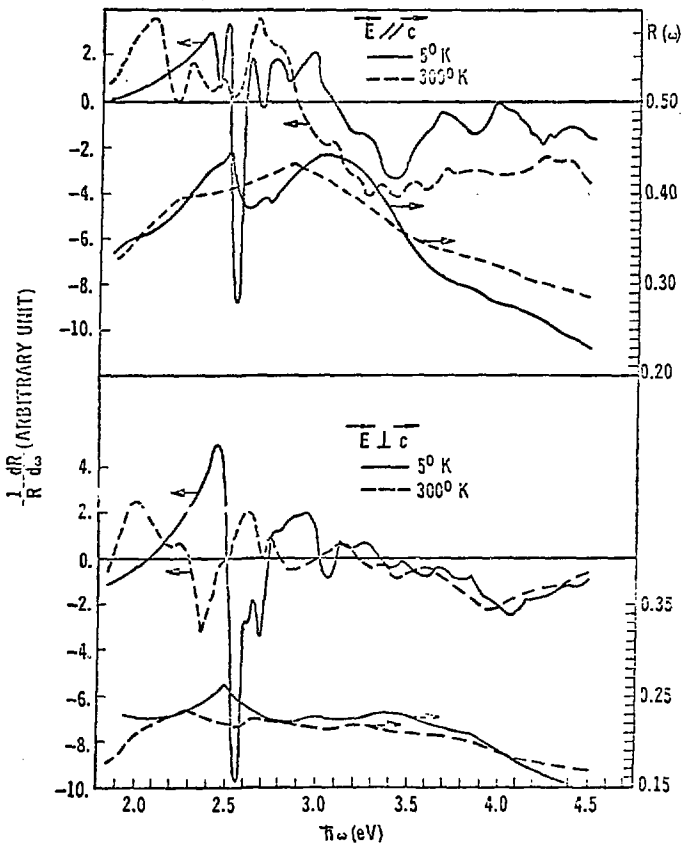
E // c
5° K
300° K
R (ω)
E ⊥ c
5° K
300° K
$\frac{1}{R}\frac{dR}{d\omega}$ (ARBITRARY UNIT)
ħω (eV)
XBL 7710-6799

FIGURE 35

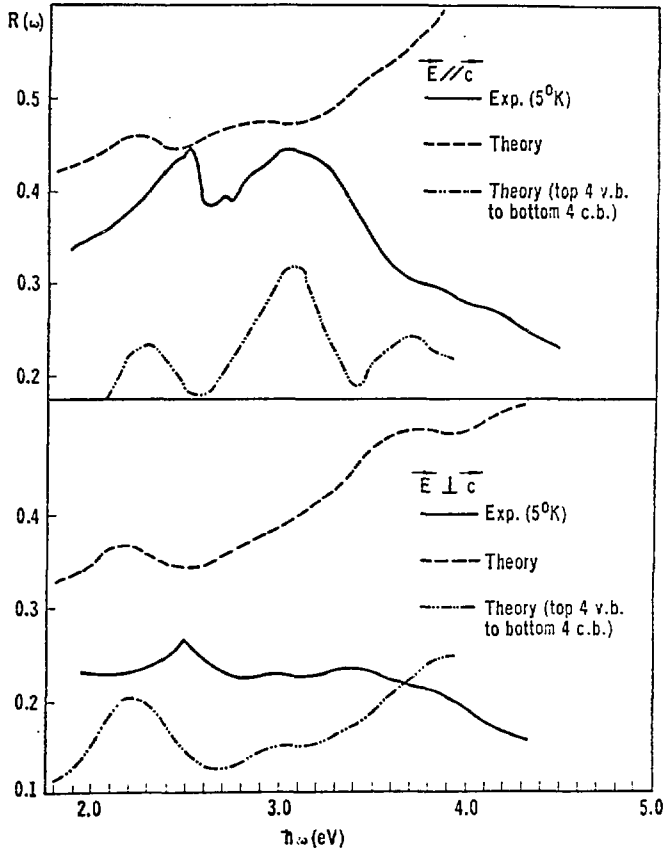
R(ω)
0.5
0.4
0.3
0.2
E // c
Exp. (5°K)
Theory
Theory (top 4 v.b. to bottom 4 c.b.)
0.4
0.3
0.2
0.1
E ⊥ c
Exp. (5°K)
Theory
Theory (top 4 v.b. to bottom 4 c.b.)
2.0
3.0
4.0
5.0
ħω (eV)
XBL 7710-6800

FIGURE 36

TABLE I

Region	Other experimental data	$\frac{1}{R}\frac{dR}{d\omega}$	$\frac{d\epsilon_2}{d\omega}$	Theory	CP symm.	Transition
(a) PbTe[a]						
E_0	0.190[a]			0.19	M_0	$L(5\rightarrow 6)$
E_1	1.24			1.07	M_1	$\Sigma(5\rightarrow 7)$
				1.27	M_0	$L(5\rightarrow 7)$
		2.16(w)[d]				
E_1	2.18[d]	2.25[d]	2.1	2.00	M_1	$\Sigma(5\rightarrow 7)$
		2.36[d]	2.2	2.03	M_2	$\Delta(5\rightarrow 6)$
	2.45[c]	2.56(w)[d]	2.3			
E_2	3.5[b]	3.47	3.3	2.78	M_2	$\Delta(4\rightarrow 6)$
		4.83(w)	4.9	3.1	M_1	$\Sigma(4\rightarrow 7)$
		5.9	5.9			
E_4	6.3[b]					
E_3	7.8[b]				Volume effects	transitions near X
E_5	11.2[b]					
(b) PbSe						
E_0	0.165[a]			0.172	M_0	$L(5\rightarrow 6)$
E_1	1.59[b]			1.6	M_0	$L(5\rightarrow 7)$
	1.54[c]	1.97(w)	2.0	1.9	M_1	$\Sigma(5\rightarrow 6)$
	1.78[a]	2.16(w)	2.15	2.3	M_0	$L(6\rightarrow 8)$
E_1	2.95[b]	2.84(w)[d]	2.65	2.7	M_1	$\Sigma(5\rightarrow 7)$
	3.12[b]	3.12[d]	2.8	2.9	M_2	$\Delta(5\rightarrow 6)$
	3.3[c]					
	3.8[c]					
E_2	4.5[b]	4.47	4.40	4.2	M_2	$\Delta(4\rightarrow 6)$
	4.6[c]	5.52	5.3	4.3	M_1	$\Sigma(4\rightarrow 7)$
E_4	7.1[b]					
E_3	9.1[b]				Volume effects	transitions near Γ and X
E_5	12.5[b]					
(c) PbS						
E_0	0.296[a]			0.287	M_0	$L(5\rightarrow 6)$
E_1	1.85[b,c]	1.9	2.0	1.6	M_0	$L(5\rightarrow 7)$
	1.98	2.25	2.1	1.9	M_1	$\Sigma(5\rightarrow 6)$
		2.45	2.3			
		2.85	2.5			
E_1	3.45[b]	3.25[d]	3.0			
	3.7[c]	3.66[d]	3.3	2.94	M_1	$\Sigma(5\rightarrow 7)$
	4.0[c]	4.01[d]	3.9(w)	3.5	M_2	$\Delta(5\rightarrow 6)$
	4.6[c]	4.5[d]				
E_2		5.08	5.0	4.92	M_1	$\Sigma(4\rightarrow 7)$
	5.27[b]	5.31	5.2	5.1	M_2	$\Delta(4\rightarrow 6)$
		5.75(w)				
E_4	8.1[b]					
E_3	9.8[b]				Volume effect	transitions near Γ and X
E_5	13.9[b]					

[a]Reference 24
[b]Reference 19
[c]Reference 21
[d]Structure in $(1/R)\,dR/d\omega$ due to structure in ϵ_1.
[e]Reference 20

Table II
Reflectivity structure

Theoretical Peak Position (eV)	Experimental Peak Position (eV) (a)	(b)	(c)	(d)	Polarization (a)	Peak	Location in zone	cp energy (eV)
		2.08†				A'	Γ_4-Γ_3	
	2.14	2.145†	2.05		⊥, ∥	B'	Γ_5-Γ_3	
		2.21†	2.11			C'		
	2.29	2.3†			⊥	B''	Γ_5-Γ_2	
	2.31				∥	C''		
2.31	2.51	2.46	2.39	2.34	∥, ⊥	A	Γ_2^--Γ_1^-	2.31*
2.27	2.63	2.53	2.46	2.40	⊥	B	Γ_1^--Γ_1^-	2.27*
2.43	2.67	2.59	2.52	2.48	∥	C	Γ_2^--Γ_1^-	2.43*
3.04					∥	$E_1(1)$	X_1-X_1(15,16-17,18)	3.04{3.05*, 3.03*
3.41	3.02	3.02	2.97	2.87 (2.92)	∥, ⊥		N_1-N_1(16-17) (0.2,0.2,0.4)	3.42*
3.37					⊥	$E_1(2)$	X_1-X_1(13,14-17,18)	3.36{3.35*, 3.37*
3.41	3.08	3.15	3.09	3.05	⊥, ∥		N_2-N_1(15-17) (0.2,0.2,0.4)	3.50*
3.6	3.2	3.22	3.13	3.32	⊥(∥)	$E_1(3)$	N_2-N_1(16,17) (0.3,0.3,0.38)	3.6
3.9	3.41	3.48	3.41	3.64	⊥	$E_1(4)$	Σ_2-Σ_1(16,18) (0.25,0.25,0)	3.95

Table II (continued)

Theoretical Peak Position (eV)	Experimental Peak Position (eV)				Polarization	Peak	Location in zone	cp energy (eV)
	(a)	(b)	(c)	(d)	(a)			
4.0	3.74	3.75	3.71	3.83 (3.72)	$\parallel(\perp)$	E_c	X_1-X_1(11,12-17,18)	3.9
4.6	4.17				$\perp$		Λ(13-17)(0,0,0.6) Σ(14-17) (0.25,0.25,0)	4.6
4.76	4.3				$\parallel$		Δ(15-17)(0.34,0,0)	4.76
4.77	4.46				$\perp$	E_2	Γ-Γ(13-18)	4.77
5.05	4.73				$\parallel$		(14-17)(0.16,0.5,0)	5.05
4.96	4.79				$\perp$		X(16-20) and along Σ	4.96
5.21	4.92 (4.93)				$\parallel(\perp)$		Δ(15-18)(0.5,0,0)	5.21

(a) This work at 5°K

(b) Thermoreflectance work of Shileika at 120°K (Ref. 28)

(c) Electroreflectance work of Shileika at 300°K (Ref. 28)

(d) Electroreflectance work of Shay at 300°K (Ref. 29)

+ Wavelength-modulated absorption work of Shileika at 77°K (Ref. 28)

* spin-orbit Hamiltonian included.

Table III

GaSe				GaS
Experiment			Theory	Correspondence
Label (this work)	Energy 5°K	Label (Ref. 18)	Assignment	Energy 5°K
S1(excit.)	3.37			4.55
S1	3.40		Γ(xy)16-19	4.61
GS1	3.58		Σ(z)18-19	
	3.70		T(z)18-19	
GS2	3.80	E_1	T,S(z)17-19	4.03
GS3	--			4.20
S2	4.07	E_2	M(z,y)15-20	4.82
G1	4.28		H(z)18-19	4.30
G2	4.41			4.42
GS4	4.54 4.67		Σ(xy)16-20 Γ(xy)16-20 T(z)17-20	4.82
S3	4.86	E_3	Σ(xy)16-20	5.57
G3	5.03		--	5.03
S4	5.13	E_3'	Σ(xy)14-20	5.78
G4	--			5.23
GS5	5.56	E_4	Σ(x,y)18-20	5.90
GS6	5.83	E_4'		6.20

Table IV

Technique or theoretical model	Ref.	$\mu_\perp$	$\mu_\parallel$
EA (ionization field)	a	0.089	
ER (ionization field)	a		0.16
ER (period of oscillations)	a	0.014-0.09	0.09
M_0 c.p. (isotr. 3-D exc.)	b	0.17	0.17
M_0 c.p. (2-D exc.)	b	0.06	∞
M_1 c.p. (hyp. exc.)	b	0.06	∞
M_0 c.p. (anis. 3-D exc.)	c	~0.17	~0.3

a) after Ref. 43, EA: electro absorption, ER: electro reflectance

b) this work, E_B = 30 meV

c) this work, E_B = 30 meV, $m_{c\parallel} = 0.3\ m_0$, $m_{c\perp} = 0.17\ m_0$ after Ref. 9.

TABLE V

SnS_2	Diff. Reflectivity	Absorption		
Reference	(This work)	(a)	(b)	(c)
300° K	2.32 eV	2.21	2.07	2.22
5° K/77° K	2.50 eV (5° K)	~ 2.40 (77° K)	-	-

a) - Ref. 50

b) - Ref. 51

c) - Ref. 53

TABLE VI : SnS_2

This work : 300° K	2.32	2.82	3.32	3.57	4.37	4.89	5.09 5.41	5.74	6.04			
Previous work : 300° K (a)	2.21			3.8		4.9		5.8		6.9		
This work : 5° K	2.5	2.61 2.70 2.81 2.90 2.95	3.37	3.61 3.80 3.92	4.17 4.53	4.98	5.22 5.32	5.58 5.85				
Label					Z1	Z2		X1				
Theory : Energy		2.7		3.9	4.49	4.65	5.40	5.91				
Assignment		$^{M}, L_{8-9}$		E_{8-9}	T_{8-9}	K_{8-9}	H_{7-9}	E, S_{6-9}				
					Sulphur (P_z) *Sulphur (S), tin (S)*			Sulphur (P_{xy}) *Sulphur (S), tin (S)*				

a) Ref. 50

TABLE VII $SnSe_2$

This work	300° K			1.92	2.88	3.52		3.79		4.09	4.27 4.46	4.76 5.06	5.58	
Previous work	300° K	0.97 (a) 1.09 (b) 1.03 (c)	1.3 (c)											
	77° K	0.98 (c)	1.3 (c)	1.97 (c)		3.6 (d)		3.9 (d)				4.9 (d)	~ 6 (d)	
This work	77° K				2.99	3.56	3.72	3.85		4.14	4.41	4.88 5.02	5.23 5.66	
	5° K			1.92	3.05	3.60 3.66	3.75	3.88 3.91	3.95 3.99	4.19 4.05	4.45 4.55	4.91 5.06	5.29 5.71	
	Label						X1	Z1	Z2	X2	X3	X4	X5	
Theory	Energy Assignment					3.70 6-9	3.70 Σ_{8-9}	Γ,K_{8-9}	3.95 R,U_{6-9}	4.15 R,U_{6-9}	4.55 Γ_{7-9}	4.90 M_{8-10}	5.55	

a) - Ref. 51

b) - Ref. 53

c) - Ref. 54

d) - Ref. 55